1 **The impact of lightning and radar reflectivity factor data assimilation on the very short**

2 **term rainfall forecasts of RAMS@ISAC: application to two case studies in Italy**

4 Stefano Federico[1], Rosa Claudia Torcasio[1], Elenio Avolio[2], Olivier Caumont[3], Mario Montopoli[1], Luca

5 Baldini[1], Gianfranco Vulpiani[4], Stefano Dietrich[1]

7   1. ISAC-CNR, via del Fosso del Cavaliere 100, Rome, Italy

8   2. ISAC-CNR, zona Industriale comparto 15, 88046 Lamezia Terme, Italy

9   3. CNRM UMR 3589, University of Toulouse, Météo-France, CNRS, 42 avenue G. Coriolis, 31057

10   Toulouse, France

11   4. Dipartimento Protezione Civile Nazionale Ufficio III - Attività Tecnico Scientifiche per la

12   Previsione e Prevenzione dei Rischi, 00189 Rome

14 **Abstract**

15 In this paper, we study the impact of lightning and radar reflectivity factor data assimilation on the

16 precipitation VSF (Very Short-term Forecast, 3 hours in this study) for two severe weather events

17 that occurred in Italy. The first case refers to a moderate and localised rainfall over central Italy

18 occurred on 16 September 2017. The second case, occurred on 9 and 10 September 2017, was very

19 intense and caused damages in several geographical areas, especially in Livorno (Tuscany) where

20 nine people died.

21 The first case study was missed by several operational forecasts, including that performed by the

22 model used in this paper, while the Livorno case was partially predicted by operational models.

23 We use the RAMS@ISAC model (Regional Atmospheric Modelling System at Institute for

24 Atmospheric Sciences and Climate of the Italian National Research Council), whose 3D-Var

25 extension to the assimilation of RADAR reflectivity factor is shown in this paper for the first time.

26 Results for the two cases show that the assimilation of lightning and radar reflectivity factor,

27 especially when used together, have a significant and positive impact on the precipitation forecast.

28 For specific time intervals, the data assimilation is of practical importance for civil protection

29 purposes because it changes a missed forecast of intense precipitation (≥ 40 mm/3h) in a correct

30 one.

31 While there is an improvement of the rainfall VSF thanks to the lightning and radar reflectivity factor

32 data assimilation, its usefulness is partially reduced by the increase of the false alarms, especially

33 when both dataset are assimilated.

34 **Keywords:** data assimilation, lightning, radar reflectivity factor, RAMS@ISAC.

36 **1. Introduction**

Initial conditions of numerical weather prediction (NWP) models are a key point for a good forecast (Stensrud and Fritsch, 1994; Alexander et al., 1999). Nowadays limited area models are operational at the kilometric scale (< 5 km) and data assimilation of observations with high spatio-temporal resolution as lightning or radar reflectivity factor[1], is crucial to correctly represent the state of the atmosphere at local scale (Weisman et al., 1997; Weygandt et al., 2008).

The assimilation of radar reflectivity factor is useful to improve the weather forecast considering the high spatio-temporal resolution of radar data.

First attempts to assimilate radar reflectivity factor are reported in Sun and Crook (1997, 1998), who expanded VDRAS (Variational Doppler Radar Analysis System) to include microphysical retrieval. Following these studies, several systems to assimilate radar observations, both Doppler velocity and reflectivity factor, were developed (Xue et al., 2003, Zhao et al., 2006; Xu et al., 2010). All these studies showed the stability and robustness of assimilating radar observations as well as the improvement of weather forecast.

In addition to direct methods, which assimilate the radar reflectivity factor adjusting the hydrometeor contents, there are indirect methods adjusting other variables. In particular, the method of Caumont et al. (2010) assimilates the relative humidity field. It consists of two different steps: a 1D retrieval of relative humidity (pseudo-profile), which depends on the radar reflectivity factor observations, followed by 3D-Var assimilation of the pseudo-profile. This method has the advantage to reduce the computational cost at the kilometric scale.

The choice of updating the moisture field directly is motivated by its greater impact on analyses and forecasts in comparison to that of hydrometeor-related quantities (e.g., Fabry and Sun, 2010).

Caumont et al. (2010) showed that the method improved the weather prediction of a heavy precipitation event in southern France and of an eight-day long assimilation cycle experiment. The method was applied in other studies (Wattrelot et al., 2014, using the AEROME model; Ridal and Dalbom, 2017; using the HARMONIE model), or modified using 4D-Var in place of 3D-Var (Ikuta and Honda, 2011; using the JNoVa model) showing its capability to improve the weather forecast. The method is also used in the operational context (Wattrelot et al., 2014).

Lightning is another important source of asynoptic data due to its ability to locate precisely the convection with few temporal gaps (Mansell et al., 2007). In the last two decades, there have been

---

[1] Throughout the paper we use the expression radar reflectivity factor, which is the quantity provided by the radar (and expressed in mm^6m^{-3} or dBz) after conversion from the received power. The radar reflectivity factor is different from reflectivity and is obtained in the special case of Rayleigh scattering. Reflectivity is not the quantity that radars usually provide and display on their screens although most of people refer to it.

attempts to assimilate lightning into meteorological models both at low horizontal resolution, which need a cumulus parameterization scheme to simulate convection, and at convection permitting scales.

First attempts to assimilate lightning in NWP models were based on relationships between lightning and rainfall rate estimated by microwave sensors on board polar-orbiting satellites (Alexander et al., 1999; Chang et al., 2001; Jones and Macpherson, 1997; Pessi and Businger, 2009). In this approach, the rainfall rate was computed as a function of the density of lightning observations and then transformed into latent heat, which was assimilated. The results of these studies showed a positive impact of the lightning data assimilation on the forecast up to 24h also for fields at the large scale, as sea-level pressure.

The study of Papadopulos et al. (2005) used lightning to locate convection and the simulated water vapour profile was nudged towards vertical profiles recorded during convective events.

Mansell et al. (2007) modified the Kain-Fritsch (Kain and Fritsch, 1993) cumulus convective scheme to force convection when/where flashes are observed while the convection scheme was not activated in the model simulation, demonstrating the potential of lightning to improve the convection forecast. A similar approach was introduced by Giannaros et al. (2016) into WRF showing the positive impact of lightning data assimilation on the precipitation forecast up to 24h for eight convective events that occurred over Greece.

Fierro et al. (2012) introduced a methodology to assimilate lightning at convection-resolving scales by modifying the water vapour mixing ratio simulated by WRF according to a function depending on the flash-rate and on the simulated graupel mixing ratio. The water vapour could be assimilated by nudging (Fierro et al., 2012) or 3D-Var (Fierro e al., 2016).

Qie et al. (2014), using WRF, adopted the methodology of Fierro et al. (2012) to assimilate ice crystals, graupel and snow, showing promising results for deep convective events in China.

Fierro et al. (2015) studied the performance of the Fierro et al. (2012) method for 67 days spanning the 2013 warm season over the CONUS giving a statistically robust estimation of the performance of the method. The computationally inexpensive lightning data assimilation method improved considerably the short-term (≤ 6h) precipitation forecast of high impact weather.

Lynn et al. (2015) and Lynn (2017) also applied the method of Fierro et al. (2012) to boost the local thermal buoyancy where/when lightning is observed. Results show that lightning data assimilation improved lightning forecast. Importantly, Lynn et al. (2015) offer an approach to address spurious convection (i.e., convection removal), which is a more challenging problem to tackle.

98   Federico et al. (2017a) implemented the methodology of Fierro et al. (2012) in RAMS@ISAC model,

99   showing the systematic and significant improvement of the precipitation forecast at the very short

100   range (3h) for twenty case studies occurred over Italy; the impact of lightning data assimilation for

101   longer forecast ranges (6h-24h; Federico et al., 2017b) showed considerable impact on the 6h

102   precipitation forecast, with smaller (negligible) effects at 12 h (24 h).

103   In this paper, we study the impact of radar reflectivity factor and lightning data assimilation on the

104   very short term (3h) rainfall prediction for two case studies in Italy. We use the method of Fierro et

105   al. (2012) to assimilate lightning and the method of Caumont et al. (2010) to assimilate the radar

106   reflectivity factor. The case studies occurred in September 2017. The first case, hereafter also

107   referred to as Serano, occurred on 16 September and was characterized by moderate-intense and

108   localized rainfall. The second case, hereafter also referred to as Livorno, occurred on 09-10

109   September, and was characterized by deep convection and very intense precipitation in several

110   parts of Italy. Even if the Livorno case occurred before the Serano case, we reverse the chronological

111   order in the discussion, ordering the event from the less to the most intense.

112   The forecast of severe events at the local scale still remains challenging because of the multitude of

113   physical processes involved over a wide range of scales (Stensrud et al., 2009). The Serano case

114   study, being localized in space, poses challenges in forecasting the exact position and timing of

115   convection initiation; the Livorno event involves the interaction between a high impact storm and

116   the complex orography of Italy, which is difficult to simulate at the local scale. For the above reasons

117   the forecast of both events was challenging, as confirmed by the poor forecast of RAMS@ISAC

118   without data assimilation. The difficulty to forecast timely and accurately the precipitation field for

119   the two case studies is the reason for choosing them as test cases.

120   This paper presents for the first time the assimilation of the total lightning (intra cloud + cloud to

121   ground) and radar reflectivity factor in RAMS@ISAC and shows how the assimilation of radar

122   reflectivity factor works together with total lighting data assimilation. Also, this paper shows that

123   the precipitation forecast using cloud scale observations over complex terrain can be accurate,

124   contributing to a number of works on the same subject.

125   The paper is organized as follows: Section 2 gives details on the synoptic environment of the case

126   studies showing daily precipitation, lightning and radar observations; Section 3 gives details on the

127   meteorological model, lightning and radar data assimilation; Section 4 shows the results for three

128   very short-term forecast (VSF), one for Serano and two for Livorno; Discussion and conclusions are

129   given in Section 5. This paper has additional material where we discuss: a) how the lightning and

radar reflectivity factors data assimilation impact the total water field evolution; b) the sensitivity of the results to the choice of key parameters of lightning data assimilation; c) the sensitivity of the results to two aspects of the radar formulation; d) the sensitivity of the results to two aspects of RAMS@ISAC setting; e) the impact of lightning data assimilation for a well predicted case study. Supplemental material gives also the form of the radar forward operator.

2. The case studies

2.1 The 16 September 2017 (Serano) case study

During the 16 September 2017 Italy was under the influence of a cyclone that developed to the lee of the Alps. The storm crossed Italy from NW to SE leaving light precipitation over most of the peninsula with moderate rainfall over Central Italy. Figure 1 shows the precipitation recorded by the Italian raingauge network on 16 September 2017. Light precipitation (< 5 mm/day) is reported by 1018 raingauges out of the 1666 stations measuring precipitation ($\geq$ 0.2 mm/day) on this day. Fourteen stations over Central Italy recorded more than 50 mm/day. The maximum precipitation was 90 mm/day in Città di Castello (Umbria Region, Figure 1). Because the meteorological radar closest to the maximum precipitation is over mount Serano (Figure 1), hereafter this event will be referred to as Serano.

The synoptic condition during the event is shown in Figure 2. At 500 hPa (Figure 2a) a trough, elongated in the SW-NE direction, extends over Western Europe and air masses are advected from SW towards western Alps. The interaction between the airflow and the Alps generates a low pressure to the lee of the Alps over Northern Italy.

The analysis at the surface (Figure 2b) shows the meteorological front represented by the equivalent potential temperature gradient between air masses advected over the Mediterranean Sea from NW and air masses advected from the South over the Tyrrhenian Sea. The advection of warm unstable air masses towards Central Italy is notable.

Infrared satellite images (Figure 3), from 00 UTC on 16 September to 00 UTC on 17 September, show that the cold front structure moved slowly from NW to SE. Interestingly, at 00 UTC on 16 September, it is apparent the well-defined cloud system over Central Italy (red circle of Figure 3a) that caused most of the daily precipitation observed between 43.50 and 45.0 N.

The well-defined cloud system over Central Italy is also shown in the radar Constant Altitude Plan Position Indicator (CAPPI) at 3 km above sea level at 02 UTC on 16 September (Figure 4). This CAPPI is formed by interpolating all the available data from the federated Italian radar network

coordinated by the Department of Civil Protection (twenty-two radars, see Section 3.3 for their positions) and it is also referred to as the national radar composite (hereafter also mosaic). Several convective cells exceeding 35 dBz can be noted over central-northern Italy. Importantly, the cloud system over Central Italy shown by the satellite infrared channel at 00 UTC (Figure 3a) and that of the radar at 02 UTC have similar positions, showing that the cloud system was active for several hours over Central Italy.

Figure 5 shows the lightning recorded by the LINET network (Betz et al., 2009) on 16 September 2017. More than 105.000 flashes were recorded; most of them occurred in the afternoon and evening, but a secondary maximum occurred in the night, from 00 UTC to 06 UTC. In this phase, more than 3000 flashes were observed over Central Italy.

2.2 The 09-10 September 2017 (Livorno) case study

During the days 09 and 10 September 2017, Italy was hit by a severe storm characterised by intense and widespread rainfall over the country. Figure 6a shows the precipitation on 09 September recorded by the Italian raingauge network. Rainfall was intense over the Alps, where the maximum daily precipitation was observed (193 mm/day), and over Liguria, with precipitation of the order of 30-50 mm/day. One station over Tuscany reported 90 mm/day, showing that intense precipitation already started over the Region. The storm on 09 September was intense: 20 raingauges reported more than 100 mm/day and 70 raingauges more than 60 mm/day. In most cases, this precipitation occurred within few hours.

The following day (see Figure 6b) had higher rainfall. Precipitation occurred mainly over Central Italy, especially over Lazio, and over Northern Italy, in particular over the North-East. In Tuscany, the two stations close to the sea, in the Livorno area, recorded about 150 mm/day mostly fallen between 00 and 06 UTC.

Synoptic conditions leading to this storm are shown in Figure 7. At 500 hPa (Figure 7a) a trough extended from Northern Europe towards the Mediterranean. The interaction between the air-masses and Western Alps generated a low pressure system to the lee of the Alps, which crossed the whole peninsula from NW to SE. It is noted the divergent flow over Central and Northern Italy that favoured upward motions.

At the surface, Figure 7b, the equivalent temperature gradient over the western Mediterranean is caused by the contrast between air masses pre-existing over the sea and air masses advected from France towards the Mediterranean. The pressure field at the surface advects air masses from the

194 South over the Tyrrhenian Sea. These warm and humid air masses feed the cyclone during its

195 development.

196 From a synoptic point of view, Livorno and Serano cases were similar and represented two cyclones

197 developing to the lee of the Alps (Buzzi and Tibaldi, 1978). However, Livorno case was more intense

198 than Serano.

199 The notable intensity of the Livorno case is confirmed by the lightning observations (Figure 8).

200 During the evening of 9 September (after 18 UTC) about 38.000 flashes were recorded by LINET. On

201 10 September about 290.000 flashes were recorded over Italy, following the movement of the storm

202 from NW to SE. There fore, more than 300.000 flashes were recorded from 18 UTC on 09 September

203 to 00 UTC on 11 September, which are more than three times those recorded for Serano.

204 Thermal infrared satellite images (channel, 10.8 micron; Figure 9) show the extension of the cloud

205 coverage every 12 hours. It is well evident that the cloud system was associated with a cold front

206 over Europe. More specifically, the satellite image at 00 UTC shows the cloud system over Livorno

207 area (red circle in Figure 9b), before the most intense precipitation period over Tuscany (00-06 UTC),

208 while Figure 9c shows the cloud system over Central Italy (orange circle), at the end of the period

209 of intense precipitation over Lazio (06-12 UTC).

210 We conclude the synoptic analysis of the case study with two CAPPI at 3 km observed by the radar

211 network of the Department of Civil Protection. The CAPPI in Figure 10a, at 00 UTC on 10 September,

212 shows the cloud system over Tuscany with reflectivity factors up to 40 dBz. Other clouds caused

213 rainfall over northern Italy. The CAPPI of Figure 10a is the last one assimilated by the 00-03 UTC VSF

214 on 10 September described in detail in Section 4.2.1.

215 Figure 10b shows the CAPPI of the national radar mosaic at 3 km above the sea level and at 06 UTC.

216 The cloud system is moving towards Central Italy with reflectivity factors up to 45 dBz. Other cloud

217 systems are apparent over northern Italy. Figures 10a-10b well represent the movement of the

218 storm towards SE and Figure 10b shows the last CAPPI assimilated by the 06-09 UTC VSF shown in

219 Section 4.2.2.

220

221 **3.Data and Methods**

222 *3.1 RAMS@ISAC and simulations set-up*

223 The RAMS@ISAC is used as NWP driver in this work. The model is based on the RAMS 6.0 model

224 (Cotton et al., 2003) with the addition of four main features, as well as a number of minor

225 improvements. First, it implements additional single moment microphysical schemes, whose

226 performance is shown in Federico (2016): among them, the WSM6 (Hong and Lim, 2006) is used in

227 this paper. Second, it predicts the occurrence of lightning following the diagnostic method of Dahl

228 et al. (2011), the implementation being discussed in Federico et al. (2014). Third, the model

229 assimilates lightning through nudging (Fierro et al., 2012, 2015; Federico et al., 2017a). Fourth, the

230 model implements a 3D-Var data assimilation system (Federico, 2013, hereafter also RAMS-3DVar),

231 whose extension to the radar reflectivity factor is presented in this paper (Section 3.3).

232 The list of the physical parameterisation schemes used in the simulations of RAMS@ISAC is shown

233 in Table 1.

234 Considering the domains and the configuration of the grids (Figure 11 and Table 2), two different

235 set-ups are used for Serano and Livorno. For the first case, we use the domains D1 and D2, while for

236 Livorno we use also the domain D3. The first domain covers a large part of Europe and extends over

237 the North Africa. Grid horizontal resolution is 10 km (R10). The second domain covers the whole

238 Italy and part of Europe and the grid has 4 km horizontal resolution (R4). The third domain covers

239 the Tuscany Region, has 4/3 km horizontal resolution (R1), and it is used for Livorno to represent

240 with higher spatial detail the precipitation field over Tuscany. The fine structures of the precipitation

241 field are smeared out over Tuscany using only domains D1 and D2. The operational implementation

242 of the RAMS@ISAC model uses the domains D1 and D2 and no refinements for specific areas of Italy

243 are used because this would require a computing power which is not currently available. Also, grid

244 refinements over Italy would require careful testing of the model performance and data assimilation

245 system, which are out of the scope of this paper.

246 All domains share the same vertical grid, which covers the troposphere and the lower stratosphere.

247 Vertical levels are more packed close to the ground. Among the 36 levels used in this paper 10 are

248 below 1 km, 14 below 2 km and 17 below 3 km. The first vertical level is at 50 m above the surface

249 in the terrain following coordinates used by RAMS@ISAC, the level 21 is at 5122 m. Above 6 km the

250 model levels are about 1000 m apart, while the maximum allowed distance between two levels is

251 1200 m. The complete list of the vertical levels is shown in the supplemental material of this paper

252 (Table S2).

253 The vertical grid is the same as the operational setting of RAMS@ISAC and is a compromise between

254 vertical resolution and computing time. The number of vertical levels will be increased to 42, starting

255 from September 2019, to better resolve the phenomena in this direction (Planetary Boundary Layer

256 processes, vertical motions, interaction between air masses and orography etc.), nevertheless the

257 current setting was successfully applied to the forecast of several heavy precipitation events over

258   Italy. A sensitivity test, using 42 vertical levels for the Livorno case, shows similar results to those

259   reported in Section 4. Details on this simulation can be found in the supplemental material of this

260   paper.

261   The nesting between the first and second domains is one-way, while the nesting between the

262   second and the third domains is two-way.

263   VSF was implemented as shown in Figure 12. First a run with R10 configuration was performed using

264   the 0.25° horizontal resolution GFS analysis/forecast cycle issued at 12 UTC as initial and boundary

265   conditions. R10 run, which started at 12 UTC on 16 September for Serano and at 12 UTC on 09

266   September for Livorno, lasted 36h and doesn't assimilate neither radar reflectivity factor nor

267   lightning. The R10 run was not updated after the acquisition of new data by the analysis system and

268   this is a limitation of the results shown in this paper. However, a sensitivity test for Livorno case

269   study showed that this limitation doesn't have a significant impact on the results presented in the

270   next section. Details on this experiment can be found in the supplemental material of this paper.

271   Starting from 12 UTC, ten VSF were performed using R4 for Serano and both R4 and R1 for Livorno.

272   The VSF lasted 9h and used R10 simulation as initial and boundary conditions (one-way nesting).

273   The 9h forecast was divided into two parts: the first six hours are the assimilation stage when

274   RAMS@ISAC simulation was adjusted by data assimilation, whereas the last three hours are the

275   forecast stage, without data assimilation. During the assimilation stage, flashes are assimilated by

276   nudging (Section 3.2), while radar reflectivity factor is assimilated every one-hour by RAMS-3DVar

277   (Section 3.3).

278   It is noted that data assimilation is performed over the domain D2 (R4) only, and the innovations

279   are transferred to the domain D3 (R1), for the Livorno case, by the two way-nesting. The domain D3

280   is used for the Livorno case to refine the resolution of the precipitation field over Tuscany and to

281   show the spatial and temporal precision of the precipitation forecast over Tuscany using data

282   assimilation. However, its usage is exceptional because, as stated above, Italy is a complex

283   orography country and grid refinements for specific areas are used only after the occurrence of the

284   event. For this reason, the domain D3 is usually not used in RAMS@ISAC and no statistics about the

285   background error are available for this grid.

286   Because lightning and radar reflectivity factor are cloud scale observations, their assimilation at

287   higher horizontal resolution by 3D-Var is foreseeable in future works.

288   The verification of the VSF for precipitation was done by visual comparison of the model output

289   with the raingauge network of the Department of Civil Protection, which has more than 3000

290   raingauges all over Italy.

291   In addition we considered the FBIAS (Frequency Bias; range [0, + ∞)), where 1 is the perfect score,

292   i.e. when no misses and false alarms occur), POD (Probability of Detection; range [0, 1], where 1 is

293   the perfect score and 0 the worst value), ETS (Equitable Threat Score; range [-1/3,1], where 1 is the

294   perfect score and 0 is a useless forecast), TS (Threat Score; range [0,1] where 1 is the perfect score

295   and 0 the worst value). Scores were computed from 2x2 dichotomous contingency tables (Wilks,

296   2006) for different rainfall thresholds and for different neighbourhood radii. Moreover,

297   performance diagrams (Roebber, 2009) were used to summarise the scores.

298

299   *3.2 Lightning data assimilation*

300   Lightning data are provided by LINET (LIghtning detection NETwork; Betz et al., 2009;

301   www.nowcast.de) which has more than 500 sensors worldwide with the greatest density over

302   Europe (more than 200 sensors). The network has a good coverage over Central Europe and

303   Western Mediterranean (from 10 W to 35 E and from 30 N to 60 N). The area of good coverage

304   includes the region considered in this paper.

305   LINET exploits the VLF/LF electromagnetic bands and provides measurements of both intra-cloud

306   (IC) and cloud to ground (CG) discharges. IC strokes are detected as long as lightning occurs within

307   120 km from the nearest sensor thanks to an optimised hardware and advanced techniques of data

308   processing (TOA-3D, Betz et al., 2004). According to Betz et al. (2009), LINET has a location accuracy

309   of 125 m for an average distance of 200 km among the sensors verified by strikes into towers of

310   known positions.

311   The good performance of the LINET network and its ability to detect IC strokes is shown in

312   Lagouvardos et al. (2009) for a storm in southern Germany, while the good performance over Italy,

313   including both CG and IC strokes, is discussed in Petracca et al. (2014).

314   The lightning data assimilation scheme is that of Fierro et al. (2012; 2014; 2015) and uses the total

315   lightning, i.e. intra-cloud plus cloud to ground flashes.

316   The method starts by computing the water vapour mixing ratio q_v:

317 $$q_v = Aq_s + Bq_s \tanh(CX)(1 - \tanh(Dq_g^{\alpha}))$$ (1)

318   where coefficients are set to A=0.86, B=0.15, C=0.30, D=0.25, α=2.2, q_s is the saturation mixing ratio

319   at the model atmospheric temperature, and q_g is the graupel mixing ratio (g kg^{-1}). *X* is the number

of total flashes (IC+CG) falling in a grid box of domain D2 (R4) in the past five minutes. The mixing ratio q_v of Eq. (1) is computed only for grid points where flashes are recorded. More specifically, for each grid point we consider the number of flashes falling in a grid box centred at the grid point in the last five minutes. The mixing ratio of Eqn. (1) is compared with that predicted by the model. If the mixing ratio of Eqn. (1) is larger than the simulated one, the latter is nudged towards the value of Eqn. (1), otherwise the modelled mixing ratio is left unchanged. This method can only add water vapour to the forecast.

The check and eventual substitution of the water vapour is performed every five minutes and it is made within the mixed phase layer zone (0 °C, -25°C), wherein electrification processes caused by the collision of ice and graupel are the most active (Takahashi 1978, Emersic and Sounders, 2010; Fierro et al., 2015).

The scheme of Fierro et al. (2012; 2015) was adapted to RAMS@ISAC in Federico et al. (2017a). In particular, the coefficient C of Eqn. (1) was rescaled from that of Fierro et al. (2012) considering the different spatio-temporal resolution of gridded lightning data; then the coefficient C was tuned (increased) by sensitivity tests considering two case studies of HyMeX-SOP1 (15 and 27 October 2012; HyMeX stands for the Hydrological cycle in the Mediterranean Experiment – First Special Observing Period occurred between 6 September and 6 November 2012; Ducroq et al., 2014). The C constant was adapted subjectively as a compromise of increasing the hits and minimising false alarms. POD and ETS scores were considered as metrics for this purpose. Then, Eqn. (1) was applied to twenty case studies of HyMeX-SOP1 giving a statistically significant (90, or 95% depending on the rainfall threshold) improvement of the RAMS@ISAC precipitation VSF (3h).

Nevertheless, a definitive statistic on the performance of rainfall VSF to nudging formulation in RAMS@ISAC is missing and further studies are needed in this direction. Also, the optimal choice of the coefficients A, B, C, D and α is case dependent.

Fierro et al (2012) applied the method using the ENTLN network, which has a detection efficiency (DE) greater than 50% for IC over Oklahoma, where the ENTLN data were used. The emphasis on IC flashes in the set-up of Fierro et al. (2012) is given because observational and model studies have provided evidence that IC flashes correlate better than CG flashes with various measures of intensifying convection (updraft strength, volume, graupel mass flux etc.; MacGorman et al. 1989; Carey and Rutledge 1998; MacGorman et al. 2005; Wiens et al. 2005; Kuhlman et al. 2006; Fierro et al. 2006; Deierling and Petersen 2008; MacGorman et al. 2011). For these reasons methods using both IC and CG flashes perform better than those using CG only, being CG flashes correlated with

352   the descent of reflectivity cores and the onset of the demise of the storm's updraft core

353   (MacGorman and Nielsen, 1991).

354   The analysis of the case studies shows that IC strokes are about 30% of the total number of strokes

355   reported by LINET. Also, the fraction of IC strokes to the total strokes depends on the position. For

356   example, for the Serano case, the fraction of IC strokes detected by LINET over the area hit by the

357   largest precipitation is more than 50% while over the Adriatic Sea it decreases to 10%.

358   It is also noted that the Detection Efficiency (DE) for IC strokes cannot be reliably compared between

359   LINET and ENTLN, because the area is different and the technical details about IC detection remain

360   unclear (type of signals, VLF/LF or VHF, discrimination IC-CG).

361   For all the above reasons the application of the Fierro method to RAMS@ISAC is not straightforward

362   and it is appropriate to study the dependence of the rainfall VSF to the nudging formulation. This

363   subject is studied in the supplemental material of this paper (Section S.3) and the results show that

364   the choice of the coefficient of Eqn. (1) used in this paper is reasonable.

365   It is finally noted that despite the limitations noted above, the lightning data assimilation, with the

366   setting of this paper, had a significant and positive impact on RAMS@ISAC rainfall VSF (Federico et

367   al., 2017a; 2017b).

368

369   *3.3 Radar data assimilation*

370   The method assimilates CAPPI of radar reflectivity factor operationally provided by the Italian

371   Department of Civil Protection (DPC). Radar data are provided over a regular Cartesian grid with 1

372   km horizontal resolution and for three vertical levels (2, 3, 5 km above the sea level). The CAPPIs at

373   2, 3, and 5km can be considered as under-sampled vertical profiles. CAPPIs are composed starting

374   from the 22 radars of the Italian Radar Network (Figure 13) 19 operating at the C-band (i.e., 5.6 GHz)

375   and 3 at X-band (i.e., 9.37 GHz). Data quality control and CAPPI composition is performed by DPC.

376   Data quality processing chain aims at identifying most of the uncertainty sources as clutter, partial

377   beam blocking and beam broadening. The radar observations are processed according to nine steps

378   detailed in Vulpiani et al. (2014), Petracca et al. (2018) and references therein.

379   Radial velocity is not assimilated into RAMS@ISAC because it is not operationally processed, the

380   scan strategy being optimized for QPE purposes. Furthermore, the implementation of a radial

381   velocity data assimilation scheme is under development in RAMS-3DVar and it is not currently

382   available for testing. For these reasons, we didn't consider the assimilation of this parameter.

383   Before entering data assimilation, the Cartesian grid is downscaled to 5 km by 5 km in order to

384   reduce the numerical cost of the data assimilation and the effect of correlated observation errors

385   (Rohn et al., 2001). Thus, the radar grid (Figure 4, for example) is a Cartesian grid with 5 km grid-

386   spacing and three vertical levels.

387   It is important to note that pure sampling of the data could result in implementation of errors (for

388   example reflectivity given by insects or birds) or extremes. Creating superobservations would

389   reduce this problem, the main drawback being the missing of very localised phenomena. While the

390   aim of this paper is to present the update of the data assimilation system of RAMS@ISAC and its

391   application to two challenging cases, the problem of using superobservations will be considered in

392   future studies because it impacts the results.

393   The methodology to assimilate radar reflectivity factor is that of Caumont et al. (2010), named

394   1D+3DVar, which is a two-step process: first, using a Bayesian approach inspired to GPROF (Goddard

395   Profiling Algorithm; Olson et al., 1996; Kummerow et al., 2001), 1D pseudo-profiles of model

396   variables are computed, then those pseudo-profiles are assimilated by 3DVar. Both steps are

397   discussed below.

398   The first step computes a pseudo-profile of relative humidity weighting the model profiles of relative

399   humidity around the radar profile (Bayesian approach). The pseudo-profile is computed by:

400
$$\mathbf{z_o^p} = \frac{\sum_i \mathbf{RH_i} W_i}{\sum_j W_j}$$
(2)

401   Where RH_i is the RAMS@ISAC vertical profile of relative humidity at a grid point inside a square of

402   50*50 km^2 centred at the radar vertical profile, W_i is the weight of each profile and $\mathbf{z_o^p}$ is the relative

403   humidity pseudo-profile. The weights are determined by the agreement between the simulated and

404   observed reflectivity factor:

405
$$W_i = \exp\left\{-\frac{1}{2}\left[\mathbf{z_o} - h_z(x_i)\right]^T \mathbf{R_z^{-1}}\left[\mathbf{z_o} - h_z(x_i)\right]\right\}$$
(3)

406   Where h_z is the forward observation operator, transforming the background column $\mathbf{x_i}$ into the

407   observed reflectivity factor. The radar forward observation operator is taken from the RIP

408   (Read/Interpolate/Plot)   software   (https://dtcenter.org/wrf-

409   nmm/users/OnLineTutorial/NMM/RIP/index.php, last access 03 March 2019) and is given in the

410   supplemental material of this paper (Section S8). It assumes a Marshall-Palmer hydrometeor size-

411   distribution, Rayleigh scattering, and depends on the mixing ratios of rain, graupel and snow.

412 The matrix $\mathbf{R_z}$ in Eqn. (3) is diagonal and its value is $n\sigma^2$, where σ is 1 dBz and n is the number of

413 available observations in the vertical profile (from 1 to 3). In this way, we give more weight to

414 vertical profiles containing more data.

415 The error of radar data is assumed small (1dBz) for two reasons: a) reflectivity data are carefully

416 checked by the Civil Protection Department; b) the performance of the control simulation, not

417 assimilating any data, is rather poor for the case studies. This setting, however, could not be optimal

418 for cases when the control forecast performs better. A sensitivity test using σ=5 dBz for the Livorno

419 case showed small differences compared to σ=1 dBz. The results of this sensitivity test are detailed

420 in the supplemental material of this paper (Section S4).

421 It is important to point out that the 50 km length-scale of the above step doesn't represent the

422 horizontal correlation length-scale of the background error, which determines the horizontal spread

423 of the innovations in the 3D-Var data assimilation (the latter length-scale is between 14 and 25 km

424 depending on the level). The 50 km length-scale is used to set a square for computing the pseudo-

425 profile of relative humidity (Eqn. (2)). This profile is given by a weighted average whose weights are

426 determined by the agreement between the simulated and observed reflectivity factor. The larger

427 the agreement the larger the weight. This distance is appropriate because the spatial error of

428 meteorological models in simulating meteorological features, for example fronts, can be of this

429 order. The control simulation of the two events considered in this paper confirms this choice.

430 The method is not able to force convection when the model has no rain, snow or graupel in a square

431 around ($50*50$ km^2) a radar profile with reflectivity factor greater than zero. In this case, the pseudo-

432 profile of relative humidity is assumed saturated above the lifting condensation level and with no

433 data below (Caumont et al., 2010).

434 It is also noted that the method is able to reduce spurious convection when the reflectivity factor is

435 simulated but not observed, because the pseudo-profile of relative humidity gives more weight to

436 the drier relative humidity profiles simulated by RAMS@ISAC inside the $50*50$ km^2 square centred

437 at the radar profile. Of course, the ability to reduce spurious convection depends on the availability

438 of dry model profiles around the specific radar profile (see the example below). Finally, if the

439 observed profile is dry and the profile simulated by RAMS@ISAC is dry too, the pseudo-profile is not

440 computed.

441 In summary, pseudo-profiles are computed for each profile of the radar grid whenever reflectivity

442 is observed or simulated.

443 The pseudo-profiles computed with the procedure introduced above, are then used as observations

444 in the RAMS-3DVar data assimilation (Federico, 2013), minimising the cost-function:

$$J(\mathbf{x})=\frac{1}{2}(\mathbf{x}-\mathbf{x}_b)^T\mathbf{B}^{-1}(\mathbf{x}-\mathbf{x}_b)+\frac{1}{2}(\mathbf{z}_o^p-h(\mathbf{x}))^T\mathbf{R}^{-1}(\mathbf{z}_o^p-h(\mathbf{x}))$$

445 (4)

446 Where $\mathbf{x}$ is the state vector giving the analysis when J is minimized, $\mathbf{x}_b$ is the background, $\mathbf{B}$ and $\mathbf{R}$

447 are the background and observations error matrices, $\mathbf{z}_o^p$ is the pseudo vertical profile computed by

448 Eqn. (2) and h is the forward observation operator transforming the state vector (RAMS@ISAC water

449 vapour mixing ratio) into observations. The cost function in RAMS-3DVar is implemented in

450 incremental form (Courtier et al., 1994) and its minimization is performed by the conjugate-gradient

451 method (Press et al., 1992). No multi-scale approach is used.

452 The background error matrix is divided into three components along the three spatial directions (x,

453 y, z). The $\mathbf{B_x}$ and $\mathbf{B_y}$ matrices account for the spatial correlation of the background error. The

454 correlations are Gaussian with length-scales between 14 and 25 km, depending on the vertical level.

455 These distances are computed using the NMC method (Barker et al., 2012) applied to the HyMeX-

456 SOP1 period. It is again stressed that the spread of the innovations along the horizontal spatial

457 directions in the 3D-Var analysis is determined by the length scales of $\mathbf{B_x}$ and $\mathbf{B_y}$ matrices.

458 The $\mathbf{B_z}$ matrix contains the error for the water vapour mixing ratio, which is the control variable used

459 in RAMS-3DVar. This error is about 2 g/kg at the surface and decreases with height. In particular, it

460 is larger than 0.5 g/kg below 4 km, and less than 0.2 g/kg above 5 km. The vertical decorrelation of

461 the background error depends on the level and can be roughly estimated in 500-2000 m. The

462 observation error matrix $\mathbf{R}$ in Eqn. (4) is diagonal and observations' errors are uncorrelated. This

463 choice is partially justified due to the sampling of radar reflectivity factor observation by choosing

464 one point every fifth grid points in both horizontal directions of the radar Cartesian grid. However,

465 correlation observations errors have significant impact on the final analysis, as shown for example

466 in Stewart et al. (2013), and different choices of the matrix $\mathbf{R}$ will be considered in future studies.

467 The value of the elements on the diagonal of $\mathbf{R}$ depends on the vertical level and are 1/4 of the

468 diagonal element of the $\mathbf{B_z}$ matrix at the corresponding height. With these settings, larger weights

469 are given to the observations than to the background and analyses strongly adjust the background

470 towards observations. $\mathbf{B_z}$ matrix is computed using the NMC method (Parrish and Derber, 1992;

471 Barker et al. 2004) applied to the HyMeX-SOP1. This choice is motivated by the fact that HyMeX-

472 SOP1 contains several heavy precipitation events over Italy and the background error matrix is

473 representative of the convective environment of the cases considered in this paper. In particular,

474   10 out of 20 declared IOP (Intense Observing Period) of HyMeX-SOP1 occurred in Italy (Ferretti et

475   al., 2014). In contrast, the period of September 2017, especially before the events selected in this

476   study was characterised by fair and stable weather conditions over Italy and the background error

477   matrix for September 2017 is less representative of the convective environment that characterise

478   the events of this paper.

479   Because it is the first time that we show the assimilation of radar reflectivity factor in RAMS@ISAC,

480   it is useful to discuss an example of analysis. We select the analysis of Livorno case study at 06 UTC.

481   The observed CAPPI at 3km above sea level is shown in Figure 10b. The corresponding CAPPI

482   simulated by the background is shown in Figure 14a. In general, the comparison between simulated

483   and observed reflectivity factor highlights the difficulty of the model to represent convection

484   properly. In particular, the model is able to represent the convection over Northern Italy but it has

485   poor performance over Sardinia, south of Sicily and over Central Italy. The difference between the

486   analysis and background relative humidity after and before the analysis is shown in Figure 14b

487   (absolute values less than 1% are suppressed in the figure for clarity). Both positive (convection

488   enhancing) and negative (convection suppressing) adjustments are found. Over Central Italy,

489   Sardinia and South of Sicily relative humidity is increased because the model doesn't simulate the

490   observed reflectivity (Figure 10b). The occurrence of this condition added most of the water vapour

491   to the RAMS@ISAC simulations for the case studies of this paper.   Over northern Italy the model is

492   partially dried for two different reasons: in the northwest of Italy because RAMS@ISAC simulates

493   unobserved reflectivity, in the north and northeast of Italy because the model simulates larger

494   values of reflectivity factor compared to the observations. The RAMS-3DVar reduces the relative

495   humidity field north from Corsica island, where the RAMS@ISAC predicted unobserved reflectivity,

496   while RAMS-3DVar didn't suppress the unobserved convection west from Sardinia because the

497   pseudo profiles computed over this area weren't appreciably drier than the background.

498   Cross correlations among different variables of the data assimilation system are neglected in this

499   study and the application of the RAMS-3DVar affects the water vapour mixing ratio only. Cross

500   correlations among different variables can improve the performance of data assimilation system,

501   and an example of their impact in the RAMS-3DVar is shown in Federico (2013). Nevertheless, the

502   impact of cross correlations among different variables in the precipitation VSF will be explored in

503   future works.

504   Since lightning data assimilation also adjusts the water vapour mixing ratio, it follows that the data

505   assimilation presented in this study adjusts only this parameter.

Despite the fact that both radar reflectivity factor and lightning adjust the water vapour mixing ratio, different impacts on the VSF can be expected *a-priori* because radar reflectivity factor and lightning are different types of observations and because they are used in different ways in the data assimilation system.

In particular, lightning is recorded when deep convection develops, while radar reflectivity factor is observed also for light stratiform rain. Flashes of ground based network, as LINET, are available over the open sea, even if with a reduced detection efficiency, while radar reflectivity factor is confined to the range of coastal radars in the network. Lightning has a seasonal dependence over Italy, with the maximum in summer and fall, while radar reflectivity factor is available in all seasons.

Also, differences in data assimilation of lightning and radar reflectivity factor play a role. In addition to the methods used to assimilate observations, lightning saturates the layer 0°C/-25°C where/when it is detected, while radar reflectivity factor can be assimilated by pseudo-profiles or by saturation above the lifting condensation level where observed reflectivity is greater than zero.

Therefore, despite both observations adjust the same model prognostic variable, which is a drawback of the methodology presented in this paper, the impacts of lighting and radar reflectivity factor is expected to be different as will be evident from the results of this paper.

There are, however, advantages using the methodology of this paper. In addition to being simple, it doesn't rely on approximate relationship between radar reflectivity factor with hydrometeors mixing ratio, leaving to the model the task of evolving the water vapour added/subtracted. Also, the impact of the data assimilation on model results are substantial (Fabry and Sun, 2010; Caumont et al., 2010), as also shown by the results of this paper.

Lightning and radar data assimilation may produce sharp gradients in vertical direction caused by the addition of water vapour to specific layers. In the case of lightning, the water vapour is added by nudging to reduce sharp gradients. However, radar data assimilation, which accounts for the largest mass of water added to RAMS@ISAC (see Section S.2 of the supplemental material), directly adjusts the water vapour into the model. Our experience with RAMS@ISAC, however, shows that results are reliable and the sudden addition of water vapour doesn't cause shocks to the model simulation, despite the notable gradients of specific humidity.

It is finally noted that the data assimilation increase/decrease the water vapour into the model depending on the cases. The eventual increase/decrease of the forecasted rainfall depends on the physical and dynamical processes occurring into the meteorological model, without any specific tuning.

538

4. Results

539

540 In this section, we discuss the most intense phase of the Serano case, 03-06 UTC on 16 September,

541 and two VSF forecasts, 00-03 UTC and 06-09 UTC on 10 September, for the Livorno case. The two

542 VSF for Livorno correspond to the most intense phase of the storm in Livorno and to a very intense

543 phase over Lazio region, Central Italy. The aim of the section is to show the notable improvement

544 given by lightning and radar reflectivity factor data assimilation to the VSF.

545 We consider four types of VSF (Table 3): a) CTRL, without radar reflectivity factor or lightning data

546 assimilation; b) LIGHT, assimilating lightning but not radar reflectivity factor; c) RAD, assimilating

547 radar reflectivity factor but not lightning; d) RADLI, assimilating both lightning and radar reflectivity

548 factor.

549 Several aspects of lightning and radar reflectivity factor data assimilation are considered in the

550 supplemental material of this paper: a) the relative contribution to the total water mass given by

551 lightning and radar reflectivity factor data assimilation (Section S.2); b) the sensitivity of the

552 precipitation VSF to the nudging formulation (Section S.3); c) the sensitivity of rainfall VSF to two

553 specific aspects of radar reflectivity factor data assimilation (Section S4); d) the sensitivity of rainfall

554 VSF to RAMS@ISAC setting (Section S5); e) the impact of lightning data assimilation for a case study

555 well predicted by the control forecast (Section S6); f) different plots of Figures 15-17 (Section S7)

556 and g) the radar forward operator used in RAMS-3DVar (Section S8).

557

558 *4.1 Serano: 03-06 UTC on 16 September 2017*

559 In this period, an intense and localised storm hit central Italy, while light precipitation occurred over

560 northern Italy (Figure 15a). Considering the storm over central Italy, 10 raingauges observed more

561 than 30 mm/3h, 6 more than 40 mm/3h, 3 more than 50 mm/3h and 1 more than 60 mm/3h, the

562 maximum observed value being 63 mm/3h.

563 The CTRL forecast, Figure 15b, misses the rainfall over central Italy and considerably underestimates

564 the precipitation area over Northern Italy, giving unsatisfactory results.

565 The assimilation of the radar reflectivity factor improves the forecast, as shown in Figure 15c. In

566 particular, RAD forecast shows localized precipitation (30-35 mm/3h) close to the area were the

567 most abundant precipitation was observed. Maximum precipitation is underestimated. Also, the

568 RAD forecast better represents the precipitation over Northern Italy compared to CTRL.

569 The rainfall forecast of LIGHT, Figure 15d, shows some improvements compared to CTRL because
570 the precipitation over central Italy has a maximum of 25-30 mm/3h, close to the area where the
571 maximum precipitation was observed. LIGHT, however, has a worse performance compared to RAD
572 because it underestimates the precipitation area over northern Italy. LIGHT underestimates the
573 maximum precipitation in central Italy.

574 The RADLI forecast, Figure 15e, has the best performance. The precipitation over central Italy is well
575 represented because the maximum rainfall (40-45 mm/3h) is in reasonable agreement with
576 observations, and also because the area of intense precipitation (> 25 mm/3h) is elongated in the
577 SW-NE direction in agreement with raingauge observations. The precipitation over northern Italy is
578 well represented by RADLI.

579 A performance diagram for 1 mm/3h and 30 mm/3h and for 4 km and 25 km neighbourhood radii
580 is shown in Figure 15f. Different radii are considered to account for the well-known double penalty
581 error (Mass et al., 2002; Mittermaier et al., 2013) caused by displacement errors of the detailed
582 precipitation forecast in convection allowing grids. RADLI has the best performance thanks to the
583 synergistic contribution of lightning and radar reflectivity factor data assimilation.

584

585 *4.2 Livorno*

586 The Livorno case study lasted for several hours starting at 18 UTC on 9 September 2017 and ending
587 more than a day later. The most intense phase in Livorno and its surroundings was observed during
588 the night between 9 and 10 September. In the following, we will show two representative VSF (3h),
589 including the most intense phase in Livorno.

590

591 *4.2.1 Livorno: 00-03 UTC on 10 September 2017*

592 This period represents the most intense phase of the storm in Livorno. In particular, the raingauge
593 close to the label A (Figure 16a) reported 151 mm/3h (Collesalvetti), while the one close to the label
594 B measured 82 mm/3h. Among the 518 raingauges reporting valid data, 75 observed more than 10
595 mm/3h, 31 more than 20 mm/3h, 17 more than 30 mm/3h, 9 more than 40 mm/3h, and 6 more
596 than 50 mm/3h.

597 The CTRL precipitation forecast is shown in Figure 16b. The forecast is poor because it misses the
598 precipitation swath from the coast towards NE. A precipitation swath is forecasted about 50 km to
599 the North of the real occurrence, but it is less wide compared to the observations.

The RAD forecast, Figure 16c, shows that the assimilation of radar reflectivity factor gives a clear improvement to the forecast. The largest precipitation in the coastal part of the swath (we searched for the maximum in the area with longitudes between 10.20E and 10.70E and latitudes between 43.10N and 43.60N) is 94 mm/3h. Another local maximum is in the southern part of the domain (label B of Figure 16a). The location of this maximum is well represented, but the forecasted value (55 mm/3h) underestimated the observed maximum (82 mm/3h).

An improvement, compared to both CTRL and RAD, is given by the assimilation of lightning (Figure 16d). The maximum value close to Livorno, i.e. in the coastal part of the swath, is 158 mm/3h. LIGHT simulation shows the local maximum in the southern part of the domain (about 50 mm/3h), but the amount is underestimated.

Figure 16e shows the RADLI rainfall forecast. The precipitation swath from coastal Tuscany towards NE is more intense compared to LIGHT and RAD. The maximum rainfall accumulated close to Livorno is 186 mm/3h. Also, the second precipitation maximum in the southern part of the domain reaches 70 mm/3h in good agreement with observations (82 mm/3h). RADLI is the only run giving a satisfactory precipitation VSF over the south-eastern Emilia Romagna (north-eastern part of the domain), to the lee of the Apennines. It is also noted that the main precipitation swath forecasted by RADLI is too broad in the direction crossing the swath compared to the observations. This is confirmed by the FBIAS of RADLI (not shown), which is more than 3 for thresholds larger than 42 mm/3h.

The performance diagram (Figure 16f) shows that LIGHT has better scores than RAD for this VSF.

4.2.2 Livorno: 06-09 UTC on 10 September 2017

In this period, the most intense precipitation occurred over the coastal part of Lazio (Figure 17a). More in detail, among the 2695 raingauges reporting valid data over the domain of Figure 17a, 307 reported more than 10 mm/3h, 132 more than 20 mm/3h, 86 more than 30 mm/3h, 66 more than 40 mm/3h, 49 more than 50 mm/3h and 35 more than 60 mm/3h. Among the 35 raingauges measuring more than 60 mm/3h, 33 were over Lazio, showing the heavy rainfall that occurred over the Region.

Some precipitation persisted over Tuscany but the rainfall is much lower compared to previous 6h (the rainfall over Tuscany between 03 and 06 UTC was very intense, not shown).

Figure 17b shows the rainfall simulated by CTRL. The forecast is unsatisfactory, mainly for the following two reasons: a) heavy precipitation is simulated over Tuscany (> 75 mm/3h), also close to

the Livorno area; b) precipitation is missed over central Italy. The rainfall over NE of Italy is well represented in space, but overestimated.

Considering the evolution of CTRL forecast for the two VSF of Livorno, we conclude that it was able to predict abundant rain over Livorno, but the rainfall forecast was delayed compared to the real occurrence. A similar behaviour was found in Ricciardelli et al. (2018) using the WRF model, showing that the results of this paper for Livorno are likely not tied to the specific model used.

The rainfall simulated by RAD (Figure 17c) clearly improves the forecast compared to CTRL. First, the precipitation over Lazio is well predicted. Second, the precipitation over Tuscany is less than for CTRL, showing the ability of radar reflectivity factor data assimilation to dry the model when it predicts reflectivity that is not observed. It is noted, however, that the area of intense rainfall (>60 mm/3h) is overestimated by RAD, which has a wet forecast. The wet bias of the RAD forecast is apparent in the representation of the rainfall VSF shown in the supplemental material of this paper (Figure S12).

LIGHT forecast, Figure 17d, shows a worse performance compared to RAD for this time period. The precipitation forecast is mainly over Tuscany, where it is overestimated, with a small precipitation spot over Lazio.

The precipitation forecast of RADLI, Figure 17e, represents very well the precipitation over Lazio, and the rainfall amount is better predicted compared to RAD. The precipitation over Sardinia is well represented by RADLI as well as the precipitation over Central Alps, giving the best results among all VSF.

Figure 17f shows the better performance of RAD compared to LIGHT for this precipitation VSF. RADLI has the best performance being closer to the upper right corner of the diagram.

To better understand the changes of the precipitation VSF to different data assimilation set-up, Figure 18 shows maps of water vapour mixing ratio averaged between 3 and 10 km at the end of the assimilation phase (06 UTC on 10 September 2017). It is important to note that those maps contain the effects of both data assimilation and model evolution.

The comparison between CTRL (Figure 18a) and RAD (Figure 18b) shows that RAD has a line of high water vapour values over Central Italy, extending over the Tyrrhenian Sea and Sardinia, which is not simulated by CTRL. This line results from both radar data assimilation and convection, which transports water vapour from lower to upper levels. The comparison between CTRL and RAD shows the substantial impact of radar reflectivity factor data assimilation on the model evolution despite

663   we are not using relationship between hydrometeors mixing ratios and radar reflectivity factor in

664   data assimilation.

665   LIGHT averaged water vapour (Figure 18c) over the Tyrrhenian Sea and west of Sicily is higher

666   compared to CTRL because of lightning data assimilation and model processes. Convection develops

667   over Tuscany, northern Lazio and NE of Italy, causing the increase of averaged water vapour in those

668   areas.

669   Because RAD and LIGHT both assimilate water vapour it is important to highlight the differences

670   between the two fields. First, LIGHT it is not able to represent a compact line of high water vapour

671   over Central Italy that, in the following hours, caused high precipitation over Lazio. Second,

672   averaged water vapour simulated by RAD is larger than for LIGHT over Central Italy, which is caused

673   by deeper convection developing in RAD than in LIGHT, as well as by the different contributions of

674   data assimilation. Finally, RADLI (Figure 18d) is similar to RAD but it shares also features with LIGHT

675   as the increase of water vapour over the Tyrrhenian Sea.

676   It is also interesting to compare vertical cross sections of relative humidity for different data

677   assimilation set-up. Figure 19 show the longitude-height cross sections of relative humidity from

678   different data assimilation configurations.

679   Comparing RAD and CTRL it is evident that the difference of the relative humidity field over the

680   Tyrrhenian Sea and western part of Italy (more specifically at longitudes between 10.5 and 12.5).

681   LIGHT shows two areas with high relative humidity: west of Corsica and over the Tyrrhenian Sea.

682   The wet area west of Corsica is caused by the assimilation of lighting (Figure 8b) and it is not

683   simulated by RAD because Corsica is not well sampled by the radar network and because of different

684   model evolutions. Lightning data assimilation also increases the humidity over the Tyrrhenian Sea

685   and over the western part of Italy, as shown by the comparison with CTRL, nevertheless its effect is

686   lower compared to radar reflectivity factor data assimilation.

687   RADLI has features of both lightning and radar reflectivity factor data assimilation.

688   So, considering the results of Figure 18 and 19 as well as the rainfall VSF, the impact of lightning and

689   radar reflectivity factor on the VSF can be very different despite they both adjust the water vapour

690   mixing ratio.

691

692   **5. Discussion and Conclusions**

693   In this paper, we showed the impact of lightning and radar reflectivity factor data assimilation on

694   the very short term precipitation forecast (3h) for two case studies occurred in Italy. We used

695   RAMS@ISAC model, whose 3DVar extension to the assimilation of radar reflectivity factor is shown

696   in this paper for the first time.

697   The first case study occurred on 16 September 2017 and it is a moderate case with localised rainfall

698   over central Italy. It was chosen because the control forecast, i.e. without radar reflectivity factor

699   or lightning data assimilation, missed the event. The second event, occurred on 9-10 September

700   2017, was characterised by exceptional rainfall over several parts of Italy. This event was partially

701   represented by the control forecast. In particular, the forecast of the event was incorrect because:

702   a) the control forecast was delayed compared to the observations; b) the control forecast missed

703   the rainfall over central Italy (Lazio Region).

704   It is important to recall that the impact of the lightning data assimilation on the precipitation

705   forecast of RAMS@ISAC was already studied for the HyMeX-SOP1 period (Federico et al., 2017a,

706   2017b), and a robust statistic is already available. The results of this study confirm the important

707   role of the lightning data assimilation on the rainfall forecast for other two case studies. However,

708   considering the assimilation of radar reflectivity factor, and its combination with lightning data

709   assimilation in RAMS@ISAC, the results of this paper are new.

710   Because we analysed only two case studies, no definitive conclusions can be derived on the

711   performance of RAMS@ISAC with radar reflectivity factor data assimilation. There are, however,

712   few points worth of mention.

713   The VSF performance of RAMS@ISAC is systematically improved by the assimilation of radar

714   reflectivity factor. This improvement is of paramount importance for some specific VSF (for example

715   for the 00-03 UTC of Livorno), when the control forecast missed the event while it was correctly

716   predicted by radar reflectivity factor data assimilation. Sometimes the improvement of reflectivity

717   factor data assimilation has less impact on the precipitation forecast, as for the period 18-21 UTC

718   on 9 September 2017 (Livorno, not shown, see the discussion paper Federico et al. (2018) for a

719   description of this VSF). This suggests that there is room for improvement for all components of the

720   VSF: observations, data assimilation, meteorological model.

721   Lightning and radar observations are different and both add value to the VSF. Some examples have

722   been shown: the light precipitation over Northern Italy for Serano is well forecasted assimilating

723   radar reflectivity factor, while it is not simulated assimilating flashes because they are too few in

724   this area to force convection; lightning data assimilation represents better the deep convection

725   occurring during the intense phase of the Livorno case (00-03 UTC), especially because it is able to

726   force convection where it occurs, reducing false alarms. The ability of lightning data assimilation to

727 reduce false alarms compared to RAD and RADLI it is shown by the fact that the ETS score for LIGHT

728 is sometimes the best among all simulations (see also the Section S2 of the supplemental material

729 of this paper). These results show also that the influence of different observations depends on the

730 meteorological situation.

731 The model configuration assimilating both radar reflectivity factor and lightning (RADLI) is able to

732 retain important features of both data assimilation. For example, the simulation of the Livorno case

733 in the phase 06-09 UTC was able to simulate the heavy precipitation over Lazio thanks to the radar

734 reflectivity factor data assimilation and the precipitation over Sardinia, as well as the moderate

735 precipitation over central Alps, thanks to lightning data assimilation.

736 The property of RADLI to retain the precipitation features of both RAD and LIGHT it is shown by the

737 POD score, which is the best, for most cases and thresholds, for RADLI.

738 Another interesting feature is the considerable improvement of the POD of RADLI compared to CTRL

739 for the lowest thresholds.

740 It is also underlined that the data assimilated, both lightning and radar reflectivity factor, are

741 available in real time and could be used for an operational implementation of the VSF.

742 It is worth noting that several sensitivity tests were conducted for the case studies, whose results

743 are shown in the supplemental material. In particular, we studied the sensitivity of the rainfall VSF

744 to: a) nudging formulation used for lightning data assimilation; b) increasing the observation error

745 of radar reflectivity factor; c) changing the shape of the searching area to compute the relative

746 humidity pseudo-profiles; d) updating IC/BC as new observations are available; e) increasing the

747 vertical resolution of RAMS@ISAC by using 42 vertical levels. All these sensitivity tests confirm the

748 findings of this paper.

749 The above results are promising and deserve future studies to better understand the role of radar

750 reflectivity factor data assimilation and its interaction with lightning data assimilation to improve

751 the precipitation forecast, especially at the very short range (0-3 h).

752 There are, however, less satisfactory aspects of assimilating both radar reflectivity factor and

753 lightning data. In particular, the wet bias of RAD and RADLI forecast is the main drawback of the

754 results of this paper. To reduce the moisture added by radar and lightning data assimilation further

755 research is needed and different approaches are possible (Fierro et al., 2016). In particular: a)

756 assimilating for a shorter time (0-6h in this paper); b) reducing the length-scales of the 3D-Var in the

757 horizontal directions to limit the spreading of the innovations, or assuming an innovation equal to

758 zero for grid points without lightning and with zero reflectivity factor; c) reducing the amount of

759 water vapour added to the model (for example reducing the values of A and B constants for lightning

760 data assimilation or relaxing the request of saturation when radar reflectivity is observed in areas

761 where the model has zero reflectivity); d) adding moisture to a shallower vertical layer.

762 It is also noted that a combination of heating and moistening could provide the same buoyancy with

763 less water vapour addition (Marchand and Fulberg, 2014) and this approach could be used in future

764 studies.

765 In addition to the acquisition of more case studies, there are two directions of future development

766 of this work. The lightning data assimilation can be formulated by 3DVar, using a strategy similar to

767 the radar reflectivity factor in which pseudo-profiles of relative humidity are first generated where

768 flashes are recorded, and then assimilated by 3DVar. This methodology was already reported in

769 Fierro et al. (2016). The assimilation of both radar reflectivity factor and lightning using RAMS-3DVar

770 will be explored in future studies.

771 Another important point to study is how long the innovations introduced by data assimilation lasts

772 in the forecast. While in this study we consider the VSF at 3h, future studies must explore longer

773 time ranges. This kind of study was performed for lightning data assimilation (Fierro et al., (2015);

774 Federico et al., 2017b; Lynn et al. (2015) among others) and for radar data assimilation (Hu et al.

775 (2006); Jones et al. (2014), among others), using a rationale similar to that used in this paper.

776 In general, the performance of the forecast and the impact of lightning and radar data assimilation

777 decrease with forecast range because boundary conditions propagate inside the domain and

778 because model errors grow and eventually become dominant. Improving the data assimilation

779 system also contributes to a longer resilience of model performance. The studies cited above

780 showed that lightning and radar data assimilation can have an impact up to 24h depending on

781 several factors (meteorological model, data assimilation, quality of the data, meteorological

782 conditions, initial and boundary conditions).

783 A study considering both radar reflectivity factor and lightning should be performed to understand

784 the resilience of the innovations introduced by data assimilation.

785

786 **ACKNOWLEDGMENTS**

787 This work is a contribution to the HyMeX program. Part of the computational time used for this

788 paper was granted by the ECMWF (European Centre for Medium range Weather Forecast)

789 throughout the special project SPITFEDE. LINET data were provided by Nowcast GmbH

790 (https://www.nowcast.de/) within a scientific agreement between H.D. Betz and the Satellite

791 Meteorological Group of CNR-ISAC in Rome.

792 This work was partially funded by the agreement between CNR-ISAC and the Italian Department of

793 Civil Protection.

794 We acknowledge three anonymous reviewers and the editor for the substantial improvement of the

795 quality of the paper in the review process.

796

797 **References**

798 Alexander, G. D., Weinman, J. A., Karyampoudi, V. M., Olson, W. S., and Lee, A. C. L.: The effect of
799 assimilating rain rates derived from satellites and lightning on forecasts of the 1993 superstorm,
800 Mon. Weather Rev., 127, 1433–1457, 1999.

801 Barker, D.M., Huang, W., Guo, Y.-R., and Xiao, Q.N.: A Three-Dimensional Variational Data
802 Assimilation System for MM5: Implementation And Initial Results, Monthly Weather Review, 132,
803 897-914, 2004.

804 Barker, D. M., Huang, X.-Y., Liu, Z., Auligné, T., Zhang, X., Rugg ,S., Ajjaji, R., Bourgeois, A., Bray, J.,
805 Chen ,Y., Demirtas, M.,. Guo, Y.-R, Henderson, T., Huang, W, Lin, H.C., Michalakes, J., Rizvi, S., and
806 Zhang, X.: The Weather Research and Forecasting (WRF) Model's Community Variational/Ensemble
807 Data Assimilation System: WRFDA. Bull. Amer. Meteor. Soc., 93, 831–843, 2012.

808 Betz, H.-D., Schmidt, K., Laroche, P., Blanchet, P., Oettinger, P., Defer, E., Dziewit, Z., and Konarski,
809 J.: LINET-an international lightning detection network in Europe, Atmos. Res., 91, 564– 573, 2009.

810 Betz, H. D., Schmidt, K., Oettinger, P., Wirz, M.: Lightning detection with 3D-discrimination of
811 intracloudandcloud-to-grounddischarges.   J.Geophys.   Res.   Lett.   31   L11108.
812 doi:10.1029/2004GL019821, 2004.

813 Buzzi, A. and Tibaldi, S.: Cyclogenesis in the lee of the Alps: A case study. Q.J.R. Meteorol. Soc., 104:
814 271-287. https://doi.org/10.1002/qj.49710444004, 1978.

815 Carey, L. D., and S. A. Rutledge: Electrical and multiparameter radar observations of a severe
816 hailstorm. J. Geophys. Res., 103, 13 979–14 000, doi:10.1029/97JD02626, 1998.

817 Caumont, O., Ducrocq, V., Wattrelot, E., Jaubert, G., and Pradier-Vabre, S.: 1D+3DVar assimilation
818 of radar reflectivity data: a proof of concept, Tellus A: Dynamic Meteorology and
819 Oceanography, 62:2, 173-187,   https://www.tandfonline.com/doi/abs/10.1111/j.1600-
820 0870.2009.00430.x, 2010.

821 Chang, D. E., Weinman, J. A., Morales, C. A., and Olson, W. S.: The effect of spaceborn microwave
822 and ground-based continuous lightning measurements on forecasts of the 1998 Groundhog Day
823 storm, Mon. Weather Rev., 129, 1809–1833, 2001.

824   Chen, C. and Cotton, W.R.: A One-Dimensional Simulation of the Stratocumulus-Capped Mixed
825   Layer, Boundary Layer Meteorology, 25, 289-321, 1983.

826   Cotton, W.R., Pielke Sr., R.A., Walko, R.L., Liston, G.E., Tremback, C.J., Jiang, H., McAnelly, R.L.,
827   Harrington, J.Y.m Nicholls, M.E., Carrio, G.G., and McFadden, J.P.: RAMS 2001: Current status and
828   future directions, Meteorology and Atmospheric Physics, 82, 5-29,2003.

829   Courtier, P., Thépaut, J. N., and Hollingsworth, A.: A strategy for operational implementation of 4D-
830   Var, using an incremental approach, Q. J. Roy. Meteorol. Soc., 120, 1367–1387, 1994.

831   Dahl, J. M. L., Höller, H., and Schumann, U.: Modeling the Flash Rate of Thunderstorms. Part II:
832   Implementation. Monthly Weather Review, 139, 3112-3124, 2011.

833   Deierling, W., and W. A. Peterse: Total lightning activity as an indicator of updraft characteristics. J.
834   Geophys. Res., 113, D16210, doi:10.1029/2007JD009598, 2008.

835   Ducrocq, V., Braud, I., Davolio, S., Ferretti, R., Flamant, C., Jansa, A., Kalthoff, N., Richard, E., Taupier-
836   Letage, I., Ayral, P.-A., Belamari, S., Berne, A., Borga, M., Boudevillain, B., Bock, O., Boichard, J.-L.,
837   Bouin, M.-N., Bousquet, O., Bouvier, C., Chiggiato, J.,   Cimini, D., Corsmeier, U., Coppola, L.,
838   Cocquerez, P., Defer, E., Delanoë, J., Di Girolamo, P., Doerenbecher, A., Drobinski, P., Dufournet, Y.,
839   Fourrié, N., Gourley, J.J., Labatut, L., Lambert, D., Le Coz, J., Marzano, F.S., Molinié, G., Montani, A.,
840   Nord, G., Nuret, M., Ramage, K., Rison, W., Roussot, O., Said, F., Schwarzenboeck, A., Testor, P., Van
841   Baelen, J., Vincendon, B., Aran, M., and Tamayo, J.: HYMEX-SOP1 The Field Campaign Dedicated to
842   Heavy Precipitation and Flash Flooding in the Northwestern Mediterranean. Bull. Amer. Meteor.
843   Soc., 95, 1083–1100, https://doi.org/10.1175/BAMS-D-12-00244.1 , 2014.

844   Emersic, C., and C. P. R. Saunders, 2010: Further laboratory investigations into the relative
845   diffusional growth rate theory of thunderstorm electrification. Atmos. Res., 98, 327–340,
846   doi:https://doi.org/10.1016/j.atmosres.2010.07.011, 2010.

847   Fabry, F., and Sun, J: For how long should what data be assimilated for the mesoscale forecasting of
848   convection and why? Part I: On the propagation of initial condition errors and their implications for
849   data assimilation. Monthly Weather Review, 138(1), 242–255, https://doi.org /2009mwr2883.1,
850   2010.

851   Federico, S.: Implementation of a 3D-Var system for atmospheric profiling data assimilation into the
852   RAMS model: Initial results, Atmospheric Measurement Techniques, 6(12), 3563-3576, 2013.

853   Federico, S.: Implementation of the WSM5 and WSM6 Single Moment Microphysics Scheme into
854   the RAMS Model: Verification for the HyMeX-SOP1, Advances in Meteorology, Volume 2016, 2016.

855   Federico, S., Avolio, E., Petracca, M., Panegrossi, G., Sanò, P., Casella, D., and Dietrich S.:Simulating
856   lightning into the RAMS model: Implementation and preliminary results, Natural Hazards and Earth
857   System Sciences, Volume 14, Number 11, p.2933-2950, 2014.

Federico, S., Petracca, M., Panegrossi, G., and Dietrich, S.: Improvement of RAMS precipitation forecast at the short-range through lightning data assimilation, Nat. Hazards Earth Syst. Sci., 17, 61–76, https://doi.org/10.5194/nhess-17-61-2017, 2017a.

Federico, S., Petracca, M., Panegrossi, G., Transerici, C., and Dietrich, S.: Impact of the assimilation of lightning data on the precipitation forecast at different forecast ranges. Adv. Sci. Res., 14, 187–194, 2017b.

Federico, S., Torcasio, R. C., Avolio, E., Caumont, O., Montopoli, M., Baldini, L., Vulpiani, G., and Dietrich, S.: The impact of lightning and radar data assimilation on the performance of very short term rainfall forecast for two case studies in Italy, Nat. Hazards Earth Syst. Sci. Discuss., https://doi.org/10.5194/nhess-2018-319, in review, 2018.

Ferretti, R., Pichelli, E., Gentile, S., Maiello, I., Cimini, D., Davolio, S., Miglietta, M. M., Panegrossi, G., Baldini, L., Pasi, F., Marzano, F. S., Zinzi, A., Mariani, S., Casaioli, M., Bartolini, G., Loglisci, N., Montani, A., Marsigli, C., Manzato, A., Pucillo, A., Ferrario, M. E., Colaiuda, V., and Rotunno, R.: Overview of the first HyMeX Special Observation Period over Italy: observations and model results, Hydrol. Earth Syst. Sci., 18, 1953–1977, https://doi.org/10.5194/hess-18-1953-2014, 2014.

Fierro, A. O., A. J. Clark, E. R. Mansell, D. R. MacGorman, S. Dembek, and C. Ziegler: Impact of storm-scale lightning data assimilation on WRF-ARW precipitation forecasts during the 2013 warm season over the contiguous United States. Mon. Wea. Rev., 143, 757–777, doi:https://doi.org/10.1175/MWR-D-14-00183.1, 2015.

Fierro, A.O., Gao, l., Ziegler, C. L., Calhoun, K. M., Mansell, E. R., and MacGorman, D. R.: Assimilation of Flash Extent Data in the Variational Framework at Convection-Allowing Scales: Proof-of-Concept and Evaluation for the Short-Term Forecast of the 24 May 2011 Tornado Outbreak. Mon. Wea. Rev., 144, 4373–4393,https://doi.org/10.1175/MWR-D-16-0053.1, 2016.

Fierro, A. O., J. Gao, C. Ziegler, E. R. Mansell, D. R. MacGorman, and S. Dembek: Evaluation of a cloud scale lightning data assimilation technique and a 3DVAR method for the analysis and short-term forecast of the 29 June 2012 derecho event. Mon. Wea. Rev., 142, 183–202, doi:10.1175/ MWR-D-13-00142.1, 2014.

Fierro, A. O., M. S. Gilmore, E. R. Mansell, L. J. Wicker, and J. M. Straka: Electrification and lightning in an idealized boundary-crossing supercell simulation of 2 June 1995. Mon. Wea. Rev., 134, 3149–3172, doi:10.1175/MWR3231.1, 2006.

Fierro, A. O., Mansell, E., Ziegler, C., and MacGorman, D.: Application of a lightning data assimilation technique in the WRFARW model at cloud-resolving scales for the tornado outbreak of 24 May 2011, Mon. Weather Rev., 140, 2609–2627, 2012.

Giannaros, T. M., Kotroni, V., and Lagouvardos, K.: WRFLTNGDA: A lightning data assimilation technique implemented in the WRF model for improving precipitation forecasts, Environ. Model. Softw., 76, 54–68, doi:10.1016/j.envsoft.2015.11.017, 2016.

Hong, S.Y., Lim, J.J.O.: The WRF single-moment 6-class microphysics scheme (WSM6). J. Korean Meteorol. Soc. 42, 129–151, 2006.

Hu, M., M. Xue, and K. Brewster: 3DVAR and cloud analysis with WSR-88D level-II data for the prediction of the Fort Worth, Texas, tornadic thunderstorms. Part I: Cloud analysis and its impact. Mon. Wea. Rev., 134, 675–698, doi:10.1175/MWR3092.1, 2006.

Ikuta, Y. and Honda, Y.: Development of 1D+4DVAR data assimilation of radar reflectivity in JNoVA. Tech. Report, 01.09–01.10. http://www.wcrp-climate.org/WGNE/BlueBook/2011/individual-articles/01_Ikuta_Yasutaka_WGNE2011_1D4DVAR.pdf, 2011.

Jones, C. D., and Macpherson, B.: A latent heat nudging scheme for the assimilation of precipitation into an operational mesoscale model, Meteorol. Appl., 4, 269–277, 1997.

Jones, T. A., J. A. Otkin, D. J. Stensrud, and K. Knopfmeier: Forecast evaluation of an observing system simulation experiment assimilating both radar and satellite data. Mon. Wea. Rev., 142, 107–124, doi:10.1175/MWR-D-13-00151.1, 2014.

Kain, J. S. and Fritsch, J. M.: Convective parameterization for mesoscale models: the Kain-Fritsch scheme. The representation of cumulus convection in numerical models, Meteor. Monogr. No. 46, Am. Meteor. Soc., Boston, 165–170, 1993.

Kuhlman, K. M., C. L. Zielger, E. R. Mansell, D. R. MacGorman, and J. M. Straka: Numerically simulated electrification and lightning of the 29 June 2000 STEPS supercell storm. Mon. Wea. Rev., 134, 2734–2757, doi:10.1175/MWR3217.1, 2006.

Kummerow, C., Hong, Y., Olson, W.S., Yang. S., Adler, R.F., McCollum, J., Ferraro, R., Petty, G., Shin. D.-B., and Wilheit, T.T.: The evolution of the Goddard profiling algorithm (GPROF) for rainfall estimation from passive microwave sensors. J. Appl. Meteor., 40, 1801–1820, 2001.

Lagouvardos, K., Kotroni, V., Betz, H.-D., and Schmidt, K.: A comparison of lightning data provided by ZEUS and LINET networks over Western Europe, Nat. Hazards Earth Syst. Sci., 9, 1713–1717, https://doi.org/10.5194/nhess-9-1713-2009, 2009.

Lynn, B. H., G. Kelman, and G. Ellrod: An evaluation of the efficacy of using observed lightning to improve convective lightning forecasts. Wea. Forecasting, 30, 405-423 doi:10.1175/ WAF-D-13-00028.1., 2015.

Lynn, B.H., 2017: The Usefulness and Economic Value of Total Lightning Forecasts Made with a Dynamic Lightning Scheme Coupled with Lightning Data Assimilation.Wea. Forecasting, 32, 645–663, https://doi.org/10.1175/WAF-D-16-0031.1 , 2017.

MacGorman, I. R. Apostolakopoulos, N. R. Lund, N. W. S. Demetriades, M. J. Murphy, and P. R. Krehbiel: The timing of cloud-to-ground lightning relative to total lightning activity. Mon. Wea. Rev., 139, 3871–3886, doi:10.1175/MWR-D-11-00047.1, 2011.

928 MacGorman, D. W. Burgess, V. Mazur, W. D. Rust, W. L. Taylor, and B. C. Johnson, 1989: Lightning
929 rates relative to tornadic storm evolution on 22 May 1981. J. Atmos. Sci., 46, 221–251, doi:10.1175/
930 1520-0469(1989)046,0221:LRRTTS.2.0.CO;2.

931 MacGorman, D.R. and K.E. Nielsen: Cloud-to-Ground Lightning in a Tornadic Storm on 8 May 1986.
932 Mon. Wea. Rev., 119, 1557–1574, https://doi.org/10.1175/1520-
933 0493(1991)119<1557:CTGLIA>2.0.CO;2, 1991.

934 MacGorman, W. D. Rust, P. Krehbiel, W. Rison, E. Bruning, and K. Wiens: The electrical structure of
935 two supercell storms during STEPS. Mon. Wea. Rev., 133, 2583–2607, doi:10.1175/MWR2994.1,
936 2005.

937 MacGorman, W. D. Rust, P. Krehbiel, W. Rison, E. Bruning, and K. Wiens: The electrical structure of
938 two supercell storms during STEPS. Mon. Wea. Rev., 133, 2583–2607, doi:10.1175/MWR2994.1,
939 2005.

940 Mansell, E. R., Ziegler, C. L., and MacGorman, D. R.: A lightning data assimilation technique for
941 mesoscale forecast models, Mon. Weather Rev., 135, 1732–1748, 2007.

942 Marchand, M., and H. Fuelberg: Assimilation of lightning data using a nudging method involving low-
943 level warming. Mon. Wea. Rev., 142, 4850–4871, doi:10.1175/MWR-D-14-00076.1, 2014.
944
945 Mass, C. F., Ovens, D., Westrick, K., and Colle, B. A.: Does increasing horizontal resolution produce
946 more skilful forecasts?, B. Am. Meteorol. Soc., 83, 407–430, 2002.

947 Mellor, G., and Yamada, T.: Development of a Turbulence Closure Model for Geophysical Fluid
948 Problems, Review of Geophysics and Space Physics, 20, 851-875, 1982.

949 Mittermaier, M., N. Roberts, and S. A. Thompson: A long-term assessment of precipitation forecast
950 skill using the Fractions Skill Score. Meteor. Appl., 20, 176–186,
951 doi:https://doi.org/10.1002/met.296, 2013.

952 Molinari, J., and Corsetti, T.: Incorporation of cloud-scale and mesoscale down-drafts into a cumulus
953 parametrization: results of one and three-dimensional integrations, Monthly Weather Review, 113,
954 485-501, 1985.

955 Olson, W. S., Kummerow, C. D. , Heymsfield, G. M., and Giglio, L.: A method for combined passive-
956 active microwave retrievals of cloud and precipitation profiles. J. Appl. Meteor., 35, 1763-1789,
957 1996.

958 Papadopoulos, A., Chronis, T.G., Anagnostou, E.N.. Improving convective precipitation forecasting
959 through assimilation of regional lightning measurements in a mesoscale model. Mon. Weather Rev.
960 133, 1961-1977, 2005.

961 Parrish, D.F., and Derber, J.C.: The National Meteorological Center's Spectral Statistical Interpolation
962 analysis system, Monthly Weather Review, 120, 1747-1763, 1992.

Pessi, A.T. and S. Businger: Relationships among Lightning, Precipitation, and Hydrometeor Characteristics over the North Pacific Ocean. J. Appl. Meteor. Climatol., 48, 833–848, https://doi.org/10.1175/2008JAMC1817.1 , 2009.

Petracca M., Casella D., Dietrich S., Milani L., Panegrossi G., Sanò P., Möhrlein M., Riso S. and Betz H.D. (2014), "Lightning strokes frequency homogenization for climatological analysis: application to LINET data records over Europe", 2nd TEA – IS Summer School, June 23 – 27, Collioure, France, 2014.

Petracca, M., L. P. D'Adderio, F. Porcù, G. Vulpiani, S. Sebastianelli, and S. Puca: Validation of GPM Dual-Frequency Precipitation Radar (DPR) rainfall products over Italy. J. Hydrometeor., 19, 907–925. https://doi.org/10.1175/JHM-D-17-0144.1., 2018.

Press, W. H., Teukolsky, S. A., Vetterling, W. T., and Flannery, B. P.: Numerical recipes in Fortran 77, second ed., Cambridge Uni- versity Press, Cambridge, 992 pp., 1992.

Qie, X., Zhu, R., Yuan, T., Wu, X., Li, W., and Liu, D.: Application of total-lightning data assimilation in a mesoscale convective system based on the WRF model, Atmos. Res., 145–146, 255–266, 2014.

Ricciardelli, E.; Di Paola, F.; Gentile, S.; Cersosimo, A.; Cimini, D.; Gallucci, D.; Geraldi, E.; Larosa, S.; Nilo, S.T.; Ripepi, E.; Romano, F.; Viggiano, M. Analysis of Livorno Heavy Rainfall Event: Examples of Satellite-Based Observation Techniques in Support of Numerical Weather Prediction. Remote Sens. 2018, 10, 1549, 2018.

Ridal, M., and Dahlbom, M.: Assimilation of multinational radar reflectivity data in a mesoscale model: a proof of concept, Journal of Applied Meteorology and Climatology, 56(6), 1739–1751, https://doi.org/10.1175/jamc-d-16-0247.1, 2017.

Roebber, P.J., 2009: Visualizing multiple measures of forecast quality. Wea. Forecasting, 24, 601-608.

Rohn, M., Kelly, G., Saunders, R. W.: Impact of a New Cloud Motion Wind Product from Meteosat on NWP Analyses and Forecasts, Monthly Weather Review, 129, 2392-2403, 2001.

Smagorinsky, J.: General circulation experiments with the primitive equations. Part I, The basic experiment, Monthly Weather Review, 91, 99-164, 1963.

Stensrud, D. J., and Fritsch, J. M.: Mesoscale convective systems in weakly forced large-scale environments. Part II: Generation of a mesoscale initial condition, Mon. Weather Rev., 122, 2068-2083, 1994.

Stensrud, D.J., M. Xue, L.J. Wicker, K.E. Kelleher, M.P. Foster, J.T. Schaefer, R.S. Schneider, S.G. Benjamin, S.S. Weygandt, J.T. Ferree, and J.P. Tuell: Convective-Scale Warn-on-Forecast System. Bull. Amer. Meteor. Soc., 90, 1487–1500, https://doi.org/10.1175/2009BAMS2795.1, 2009.

Stewart, L. M., Dance, S. L., Nichols, N. K.: Data assimilation with correlated observation errors: experiments with a 1-D shallow water model, Tellus A: Dynamic Meteorology and Oceanography, 65:1, DOI: 10.3402/tellusa.v65i0.19546, 2013.

Sun, J., and Crook, N. A.: Dynamical and Microphysical Retrieval from Doppler RADAR Observations Using a Cloud Model and Its Adjoint, Part I: Model Development and Simulated Data Experiments, J. Atmos. Sci., 54, 1642–1661, 1997.

Sun, J., and Crook, N. A.: Dynamical and Microphysical Retrieval from Doppler RADAR Observations Using a Cloud Model and Its Adjoint, Part II: Retrieval Experiments of an Observed Florida Convective Storm, J. Atmos. Sci., 55, 835–852, 1998.

Takahashi, T.: Riming electrification as a charge generation mechanism in thunderstorms. J. Atmos. Sci., 35, 1536–1548, doi:https://doi.org/10.1175/1520 0469(1978)0352.0.CO;2, 1978.

Vulpiani, G., A. Rinollo, S. Puca, and M. Montopoli: A quality-based approach for radar rain field reconstruction and the H-SAF precipitation products validation. Proc. Eighth European Radar Conf., Garmish-Partenkirchen, Germany, ERAD, Abstract 220, 6 pp., http://www.pa.op.dlr.de/erad2014/programme/ ExtendedAbstracts/220_Vulpiani.pdf (last access January 2019), 2014.

Walko, R.L., Band, L.E., Baron, J., Kittel, T.G., Lammers, R., Lee, T.J., Ojima, D., Pielke Sr., R.A., Taylor, C., Tague, C., Tremback, C.J., and Vidale, P.L.: Coupled Atmosphere-Biosphere-Hydrology Models for environmental prediction, Journal of Applied Meteorology, 39, 931-944, 2000.

Wattrelot, É., Caumont, O. and Mahfouf, J. F.: Operational implementation of the 1D+3D-Var assimilation method of radar reflectivity data in the AROME model. Monthly Weather Review, 142(5), 1852–1873. https://doi.org/10.1175/MWR-D-13-00230.1, 2014.

Weisman, M. L., Skamarock, W. C., and Klemp, J. B.: The resolution dependence of explicitly modeled convective systems, Mon.Weather Rev., 125, 527–548, 1997.

Weygandt, S. S., Benjamin, S. G., Hu, M., Smirnova, T. G., and Brown, J. M.: Use of lightning data to enhance radar assimilation within the RUC and Rapid Refresh models. Third Conf. on Meteorological Applications of Lightning Data, 20–24 January 2008, New Orleans, LA, Amer. Meteor. Soc., 8.4, available at: https://ams.confex.com/ams/88Annual/webprogram/Paper134112.html (last access: 03 October 2018), 2008.

Wiens, K. C., S. A. Rutledge, and S. A. Tessendorf, A: The 29 June 2000 supercell observed during STEPS. Part II: Lightning and charge structure. J. Atmos. Sci., 62, 4151–4177, doi:10.1175/JAS3615.1, 2005.

Xu, Q., Wei, L., Gu, W., Gong, J., and Zhao, Q.: A 3.5-dimensional variational method for Doppler radar data assimilation and its application to phased array radar observations, Adv. Meteorol., vol. 2010, Article ID 797265, https://doi.org/10.1155/2010/797265, 2010.

1032 Xue, M., Wang, D., Gao, J., Brewster, K., and Droegemeier, K. K: The Advanced Regional Prediction
1033 System (ARPS), storm scale numerical weather prediction and data assimilation, Meteor. Atmos.
1034 Phys., 82, 139–170, 2003.

1035 Zhao, Q., Cook, J., Xu, Q., and Harasti, P. R.: Using radar wind observations to improve mesoscale
1036 numerical weather prediction, Weather Forecast, 21, 502–522, 2006.

1037

1038 **TABLES**

1039 Table 1: RAMS@ISAC physical parameterisations used in this paper.

Physical parameterization	Selected scheme
Parametrized cumulus convection	Modified Kuo scheme to account for updraft and downdraft (Molinari and Corsetti, 1985). The scheme is applied to R10 only.
Explicit precipitation parameterization	Bulk microphysics with six hydrometeors (cloud, rain, graupel, snow, ice, water vapour). Described in Hong and Lim (2006).
Exchange between the surface, the biosphere and atmosphere.	LEAF3 (Walko et al., 2000). LEAF includes prognostic equations for soil temperature and moisture for multiple layers, vegetation temperature and surface water, and temperature and water vapour mixing ratio of canopy air.
Sub-grid mixing	The turbulent mixing in the horizontal directions is parameterised following Smagorinsky (1963), vertical diffusion is parameterised according to the Mellor and Yamada (1982) scheme, which employs a prognostic turbulent kinetic energy.
Radiation scheme	Chen-Cotton (Chen and Cotton, 1983). The scheme accounts for condensate in the atmosphere.

1040

1041 Table 2: Basic parameters of the RAMS@ISAC grids (R10, R4 and R1, corresponding, respectively, to the domains D1, D2
1042 and D3). NNXP is the number of grid points in the WE direction, NNYP is the number of grid-points in the NS direction,
1043 NNZP is the number of vertical levels, DX is the size of the grid spacing in the WE direction, DY is the grid spacing in the
1044 SN direction. Lx, Ly, and Lz are the domain extensions in the NS, WE, and vertical directions. CENTLON and CENTLAT are
1045 the coordinates of the grid centres.

1046

	R10, D1	R4, D2	R1, D3
NNXP	301	401	203
NNYP	301	401	203
NNZP	36	36	36
Lx	3000 km	1600 km	~270 km

Ly	3000 km	1600 km	~270 km
Lz	~22400 m	~22400 m	~22400 m
DX	10 km	4 km	4/3 km
DY	10 km	4 km	4/3 km
CENTLAT (°)	43.0 N	43.0 N	43.7 N
CENTLON (°)	12.5 E	12.5 E	11.0 E

Table 3: Types of simulations performed.

Experiment	Description	Data assimilated	Model variable impacted
CTRL	Control run	None	None
RAD	RADAR data assimilation	Reflectivity factor CAPPI (RAMS-3DVar)	Water vapour mixing ratio
LIGHT	Lightning data assimilation (A=0.85; B=0.16 in Eqn. (1))	Lightning density (nudging)	Water vapour mixing ratio
RADLI	RADAR + lightning data assimilation (A=0.86; B=0.15 in Eqn (1))	Reflectivity factor CAPPI (RAMS-3DVar) + Lightning density (nudging)	Water vapour mixing ratio

1072

1073

1074 Figure 1: Daily precipitation over Italy on 16 September 2017. Only raingauges observing at least 0.2 mm/day are shown.
1075 The first number in the figure title within brackets represents the available raingauges, while the second number
1076 represents raingauges observing at least 0.2 mm/day. The lowest precipitation class is represented by smaller dots, the
1077 largest by a red square. The locations of Città di Castello and Mount Serano are indicated.
1078

1079

1080

1081

1082

1083

1084

1085

1086

1087

1088

1089

1090   a)
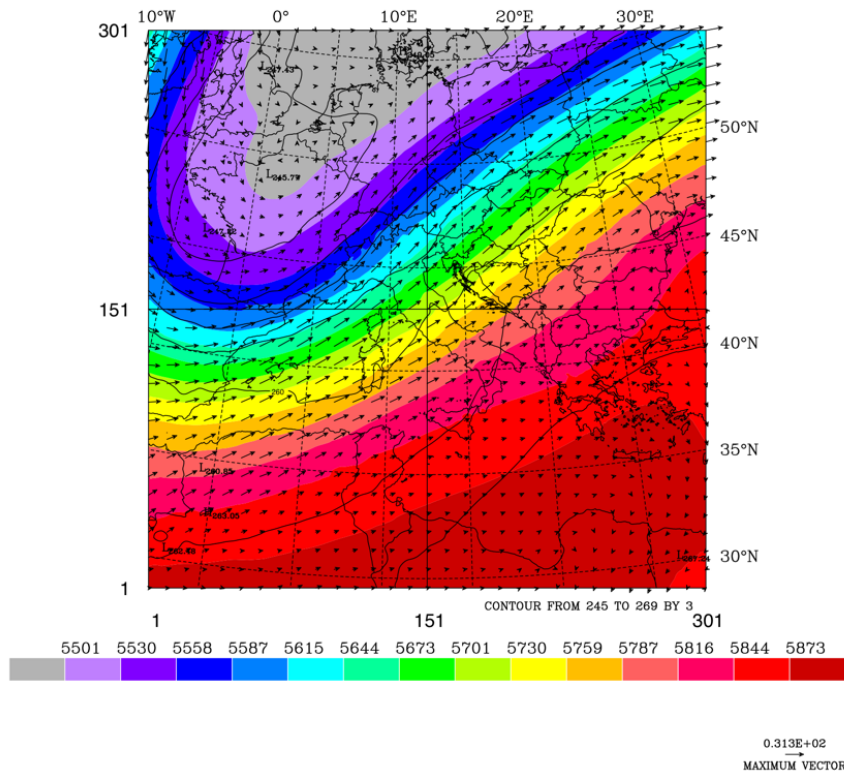
1091

1092   b)
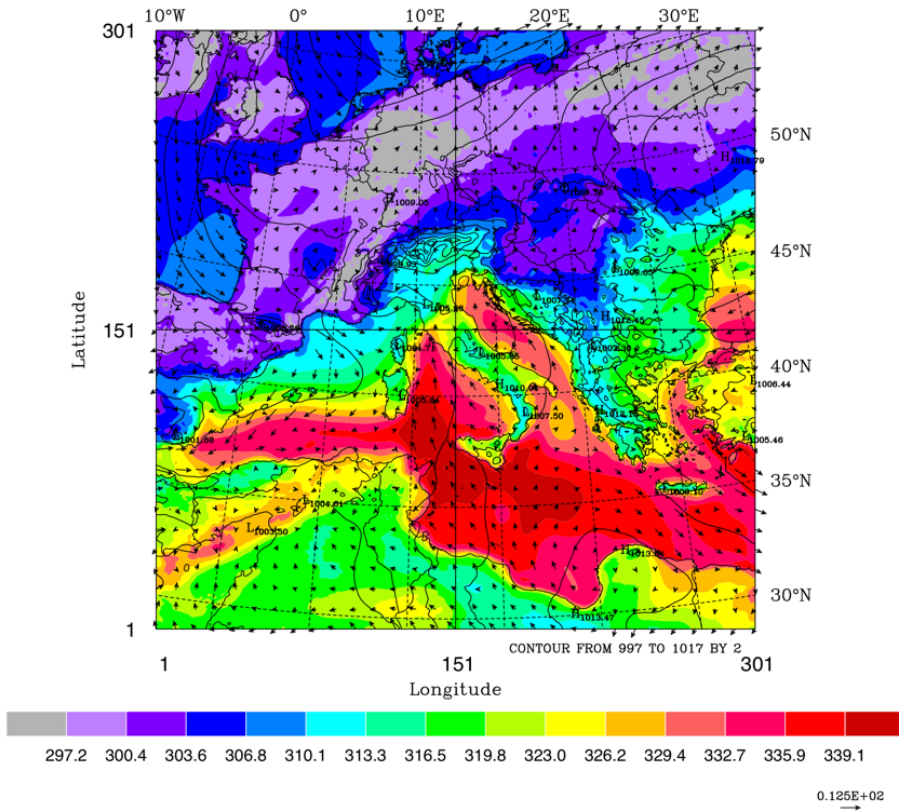
1093

1094 Figure 2: a) Geopotential height (filled contours), temperature (contours) and wind vectors at 500 hPa on 16 September
1095 2017 at 00 UTC. Maximum velocity is 31 m/s; b) equivalent potential temperature (filled contours), sea-level pressure
1096 (contours) and wind vectors at 24 m above the surface (maximum value 13 m/s). A low-pressure patter is forming over
1097 northern Italy, with a front in the western Mediterranean.
1098

a)   b)   c)

00UTC 16 sep   *12UTC 16 sep*   *00UTC 17 sep*
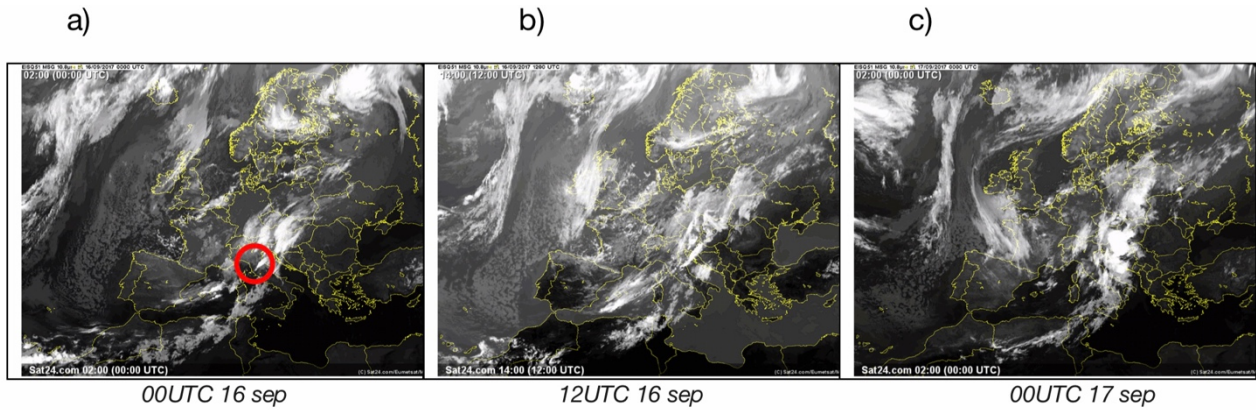
1099
1100
1102 Figure 3: a) Satellite images (METEOSAT second generation) of the infrared channel, 10.8 micron, at 00 UTC and 12 UTC
1103 on 16 September, and at 00 UTC on 17 September 2017. A well-defined cloud system is apparent inside the red circle
1104 of the image at 00 UTC on 16 September 2017.

1105
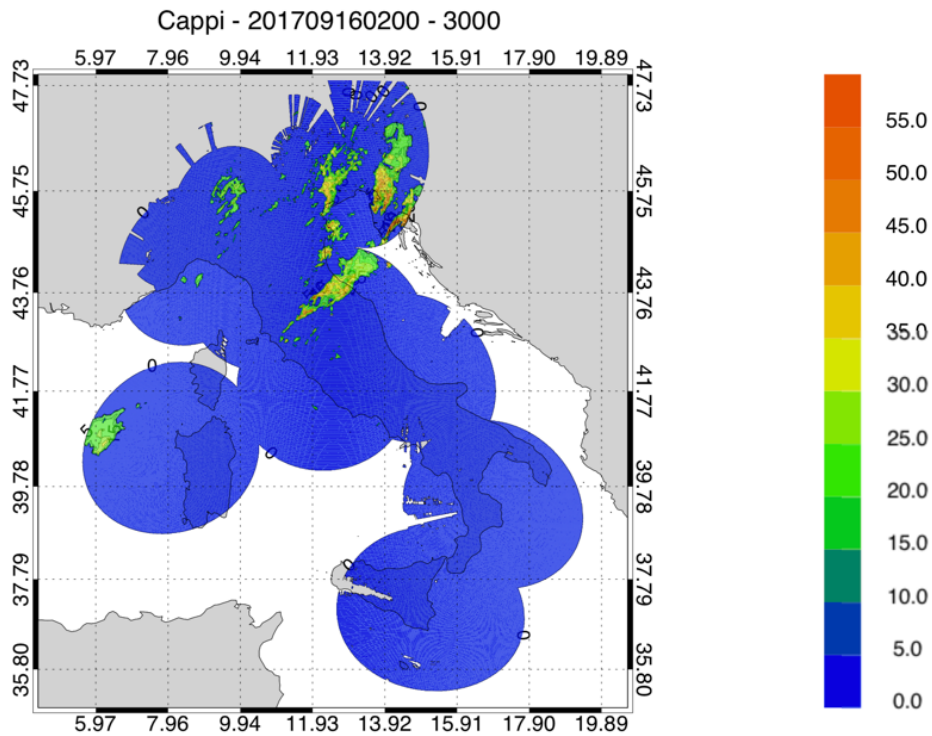
1106

1107 Figure 4: National radar mosaic at 3 km above the sea level observed at 02 UTC on 16 September 2017.

1108
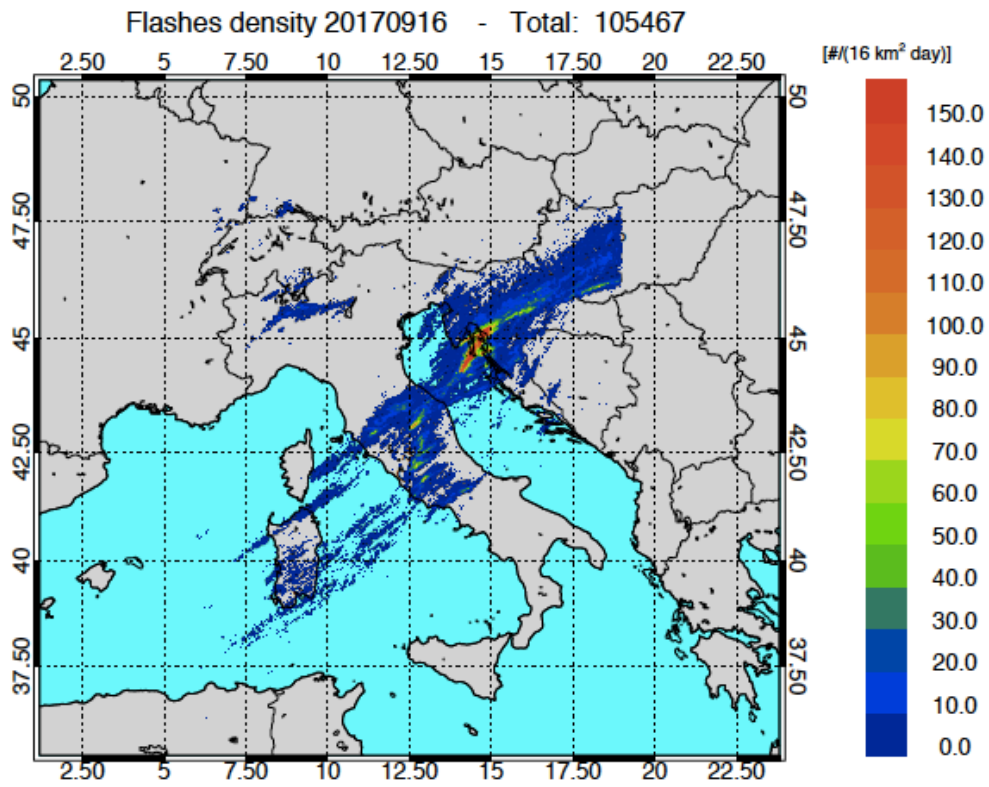
1109

Figure 5: Lightning density (number of lighting per 16 km² for the whole day) recorded on 16 September 2017. The total number of flashes is shown in the title.

a)
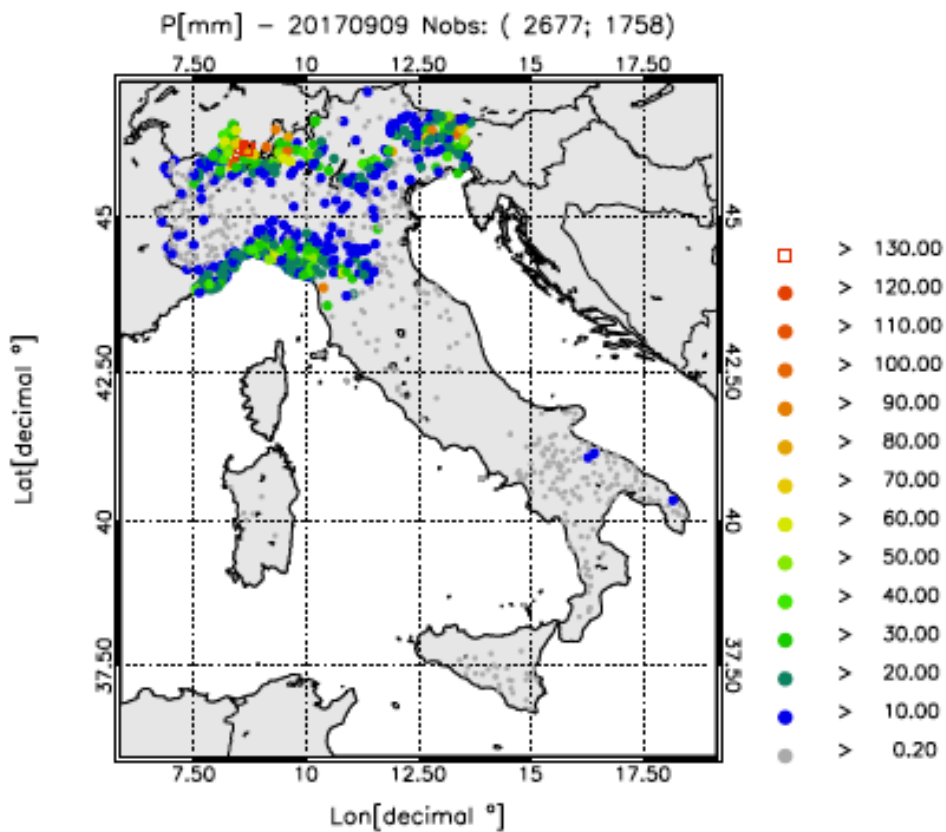
1113

1114   b)
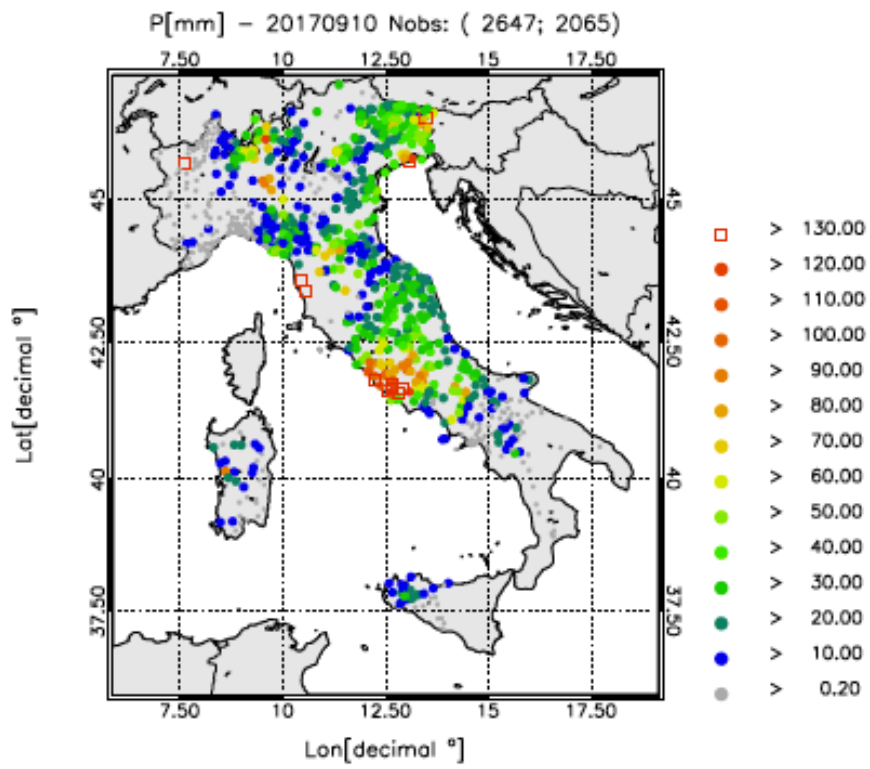
1115

1116   Figure 6: a) As in Figure 1 but for a) 9 September 2017 and b) 10 September 2017.
1117
1118
1119   a)
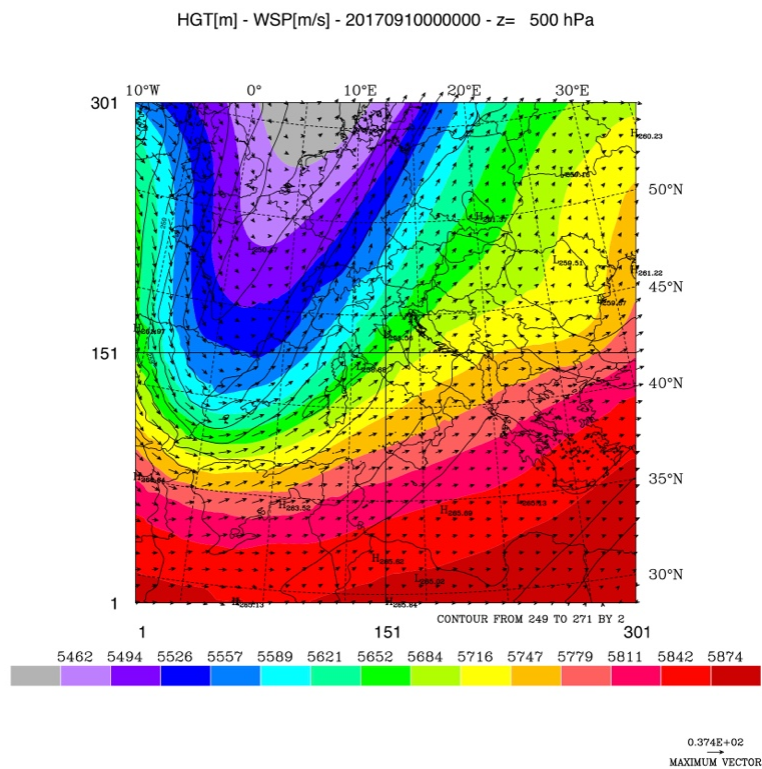
1120

1121   b)
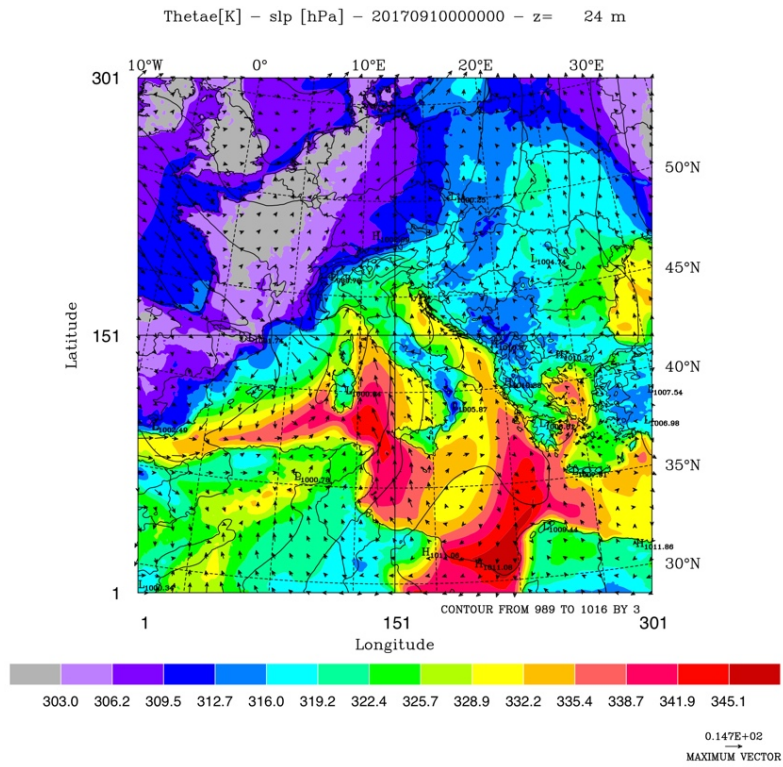
1122

Figure 7: a) Geopotential height (filled contours), temperature (contours) and wind vectors at 500 hPa at 00 UTC on 10 September 2017. Maximum velocity is 37 m/s; b) equivalent potential temperature (filled contours), sea-level pressure (contours) and wind vectors at 24 m above the surface (maximum value 15 m/s).

1123
1124
1125
1126

1127   a)
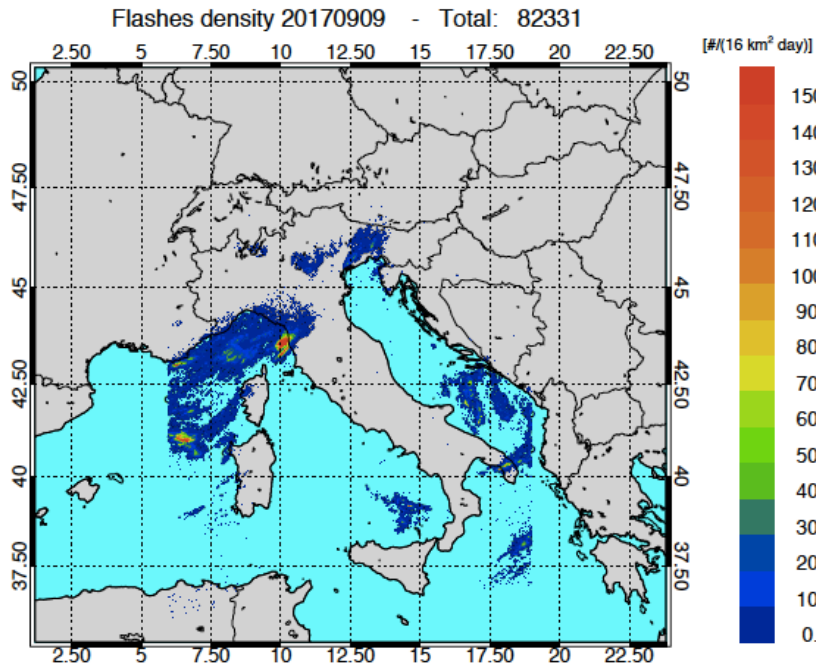
1128

1129

1130

1131   b)
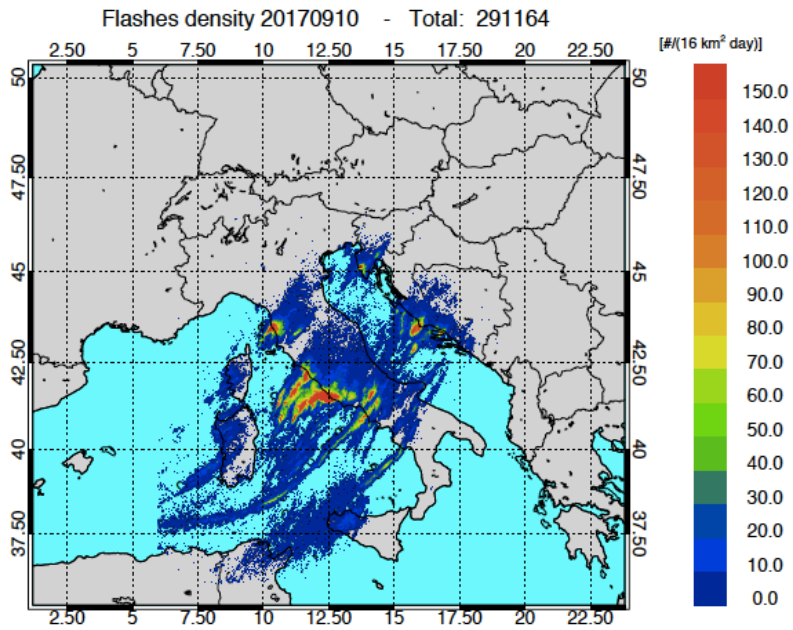
1132

Figure 8: a) Lightning density (lightning number per 16 km^2 for the whole day) recorded on 09 September 2017; b) as in
a) for 10 September 2017. The number of flashes on each day is shown in the title.

1133
1134

1135
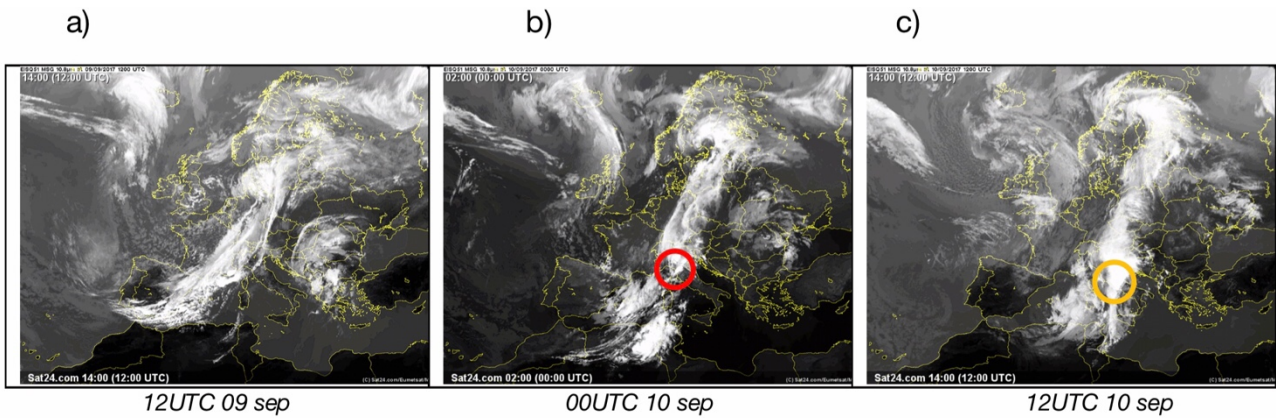
1136
1138 Figure 9: a) Satellite images (METEOSAT second generation) of the infrared channel, 10.8 micron, at 12 UTC on 9
1139 September 2017, at 00 UTC and 12 UTC on 10 September 2017. The red circle in Figure 9b and the orange circle in Figure
1140 9c show the Livorno and Lazio area, respectively.

1141

1142

1143

1144

1145

1146

1147

1148

1149

1150   a)
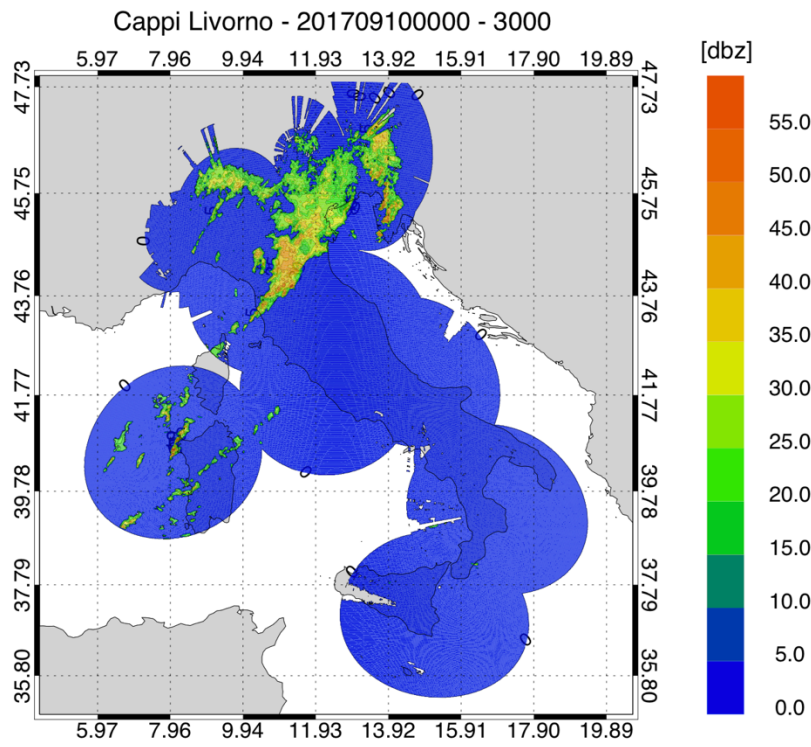
1151

1152   b)
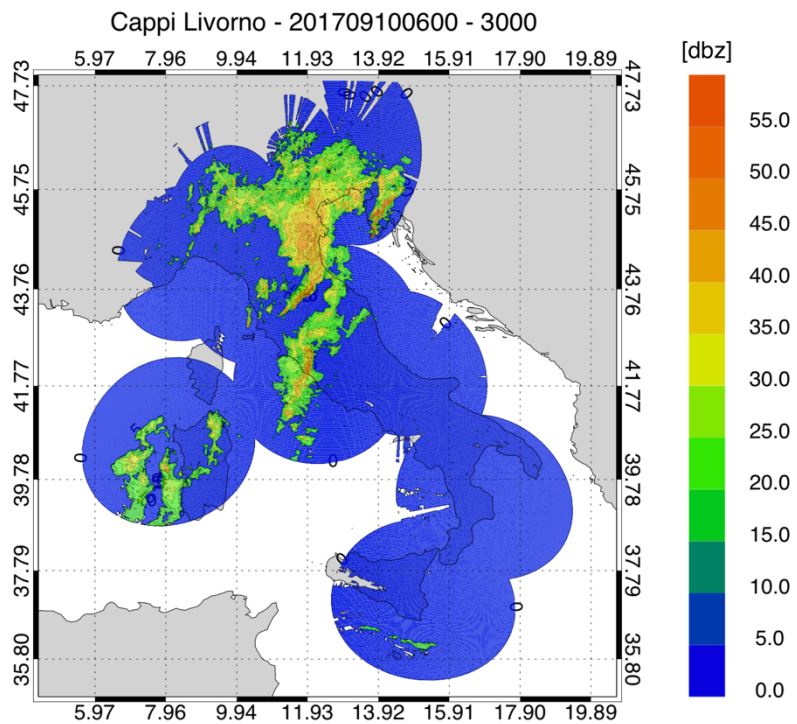
1153

1154   Figure 10: a) National radar mosaic at 3 km above the sea level observed at 00 UTC on 10 September 2017; b) as in a)
1155   at 06 UTC.

1156
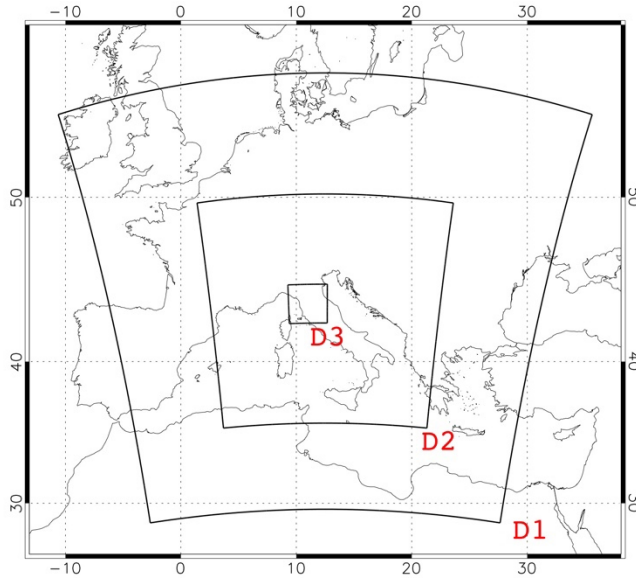
1157

1158 Figure 11: The three domains used in RAMS@ISAC. The model grid over domain D1 has 301 grid points in the NS and
1159 WE directions and has 10 km horizontal resolution, the model grid over domain D2 has 401 grid points in the NS and
1160 WE directions and has 4 km horizontal resolution. The model grid over domain D3 has 203 grid points in the NS and WE
1161 directions and has 4/3 km horizontal resolution. All grids have the same thirty-six vertical levels spanning the 0-22.4 km
1162 vertical layer.
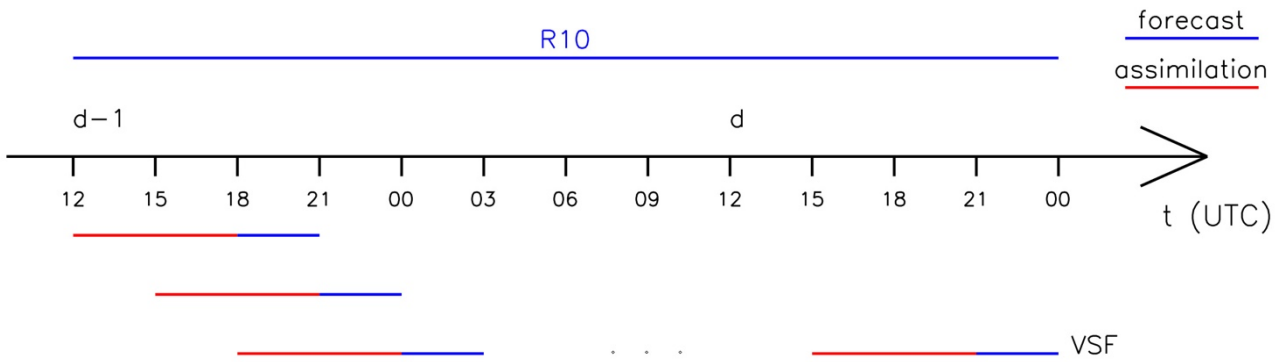
1163

1164 Figure 12: The implementation of RAMS@ISAC very short-term forecast.

1165

Figure 13: The radar network of the Department of Civil Protection. Green radars operate with dual-polarisation, blue radars have single polarisation.

1186 a)
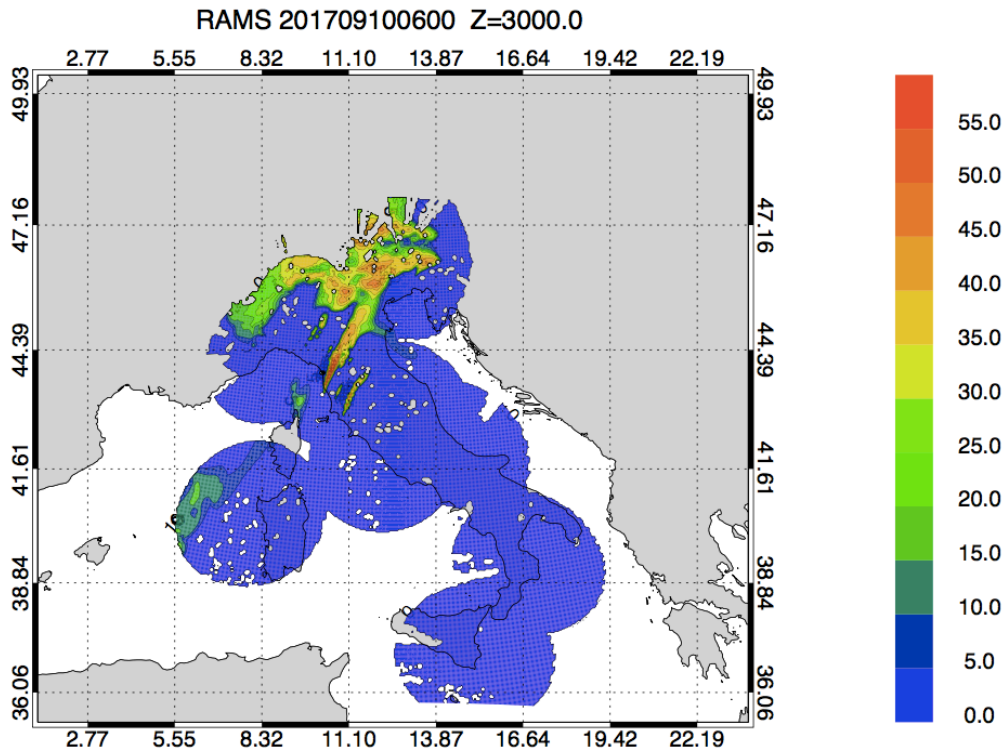
1187
1188 b)
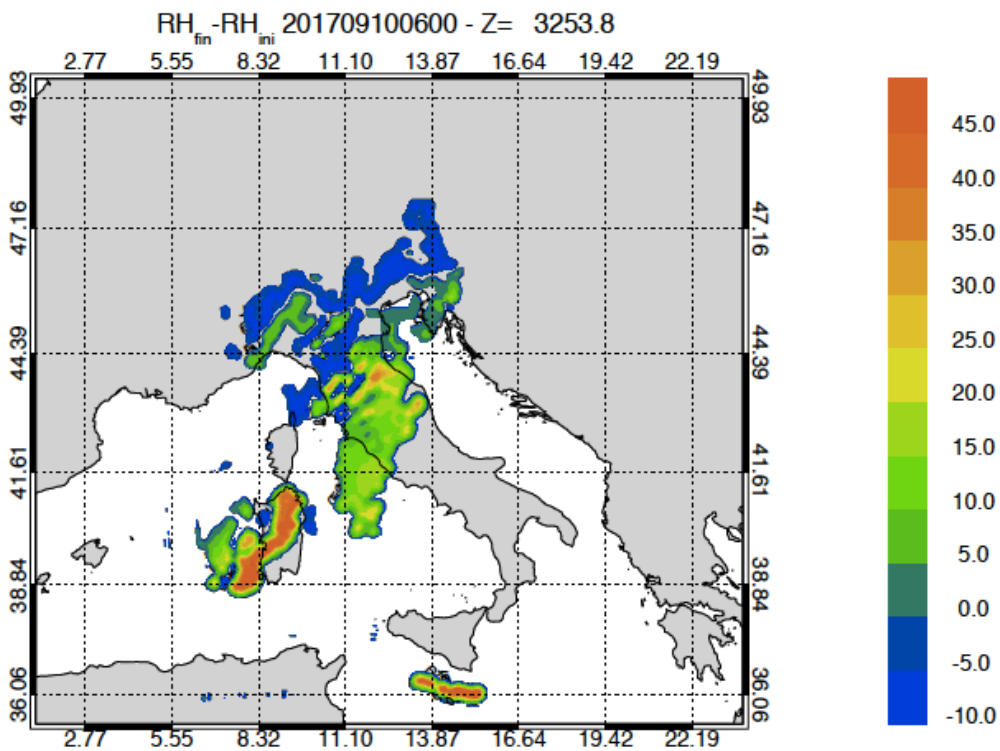
1189

1190 Figure 14: a) RAMS@ISAC reflectivity factor simulated 3 km above sea level at 06 UTC on 10
1191 September 2017; b) relative humidity difference between the analysis and the background at 06
1192 UTC at 3.2 km level in the terrain following vertical coordinate of RAMS@ISAC.
1193
1194

1195   a)
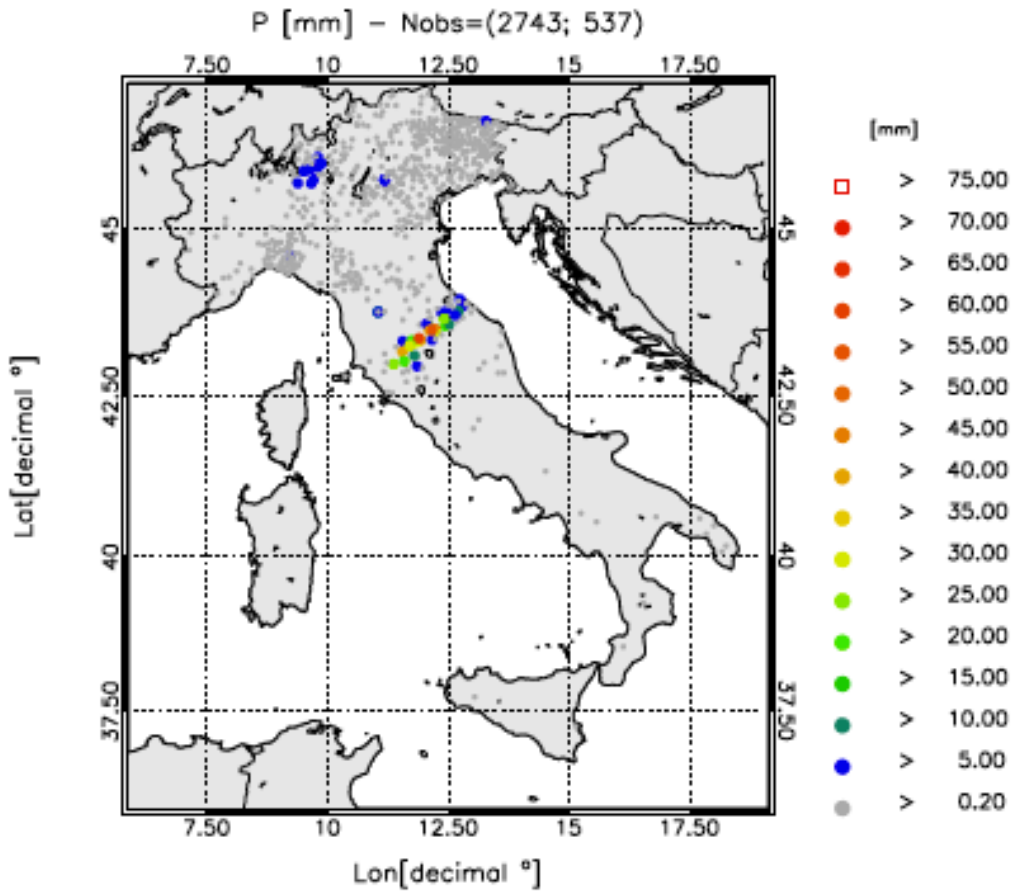
1196
1197

1198   b)
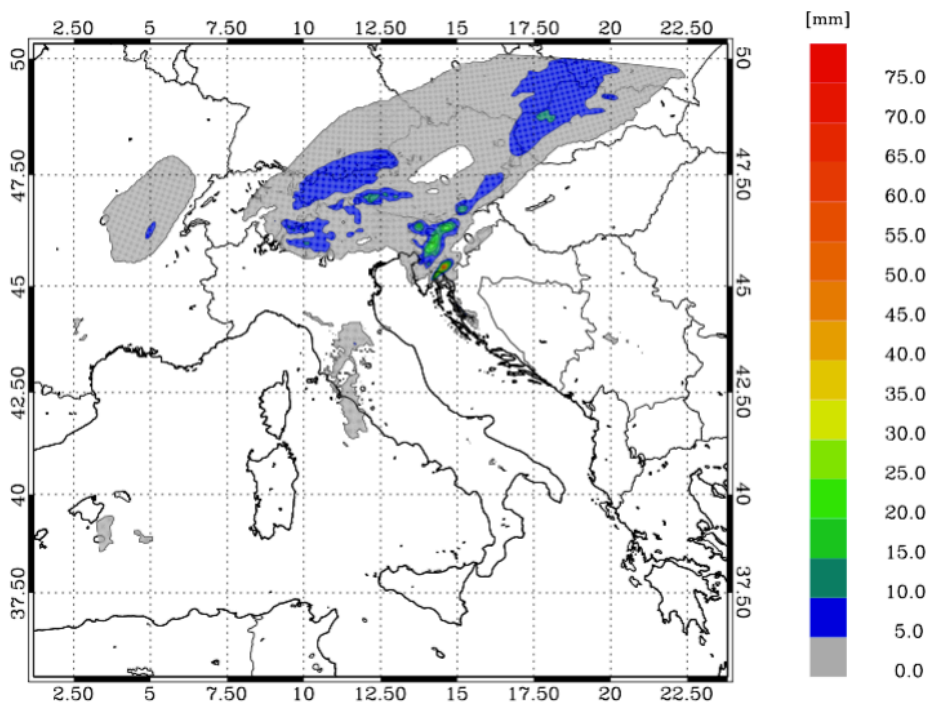
1199
1200

1201   c)

1202
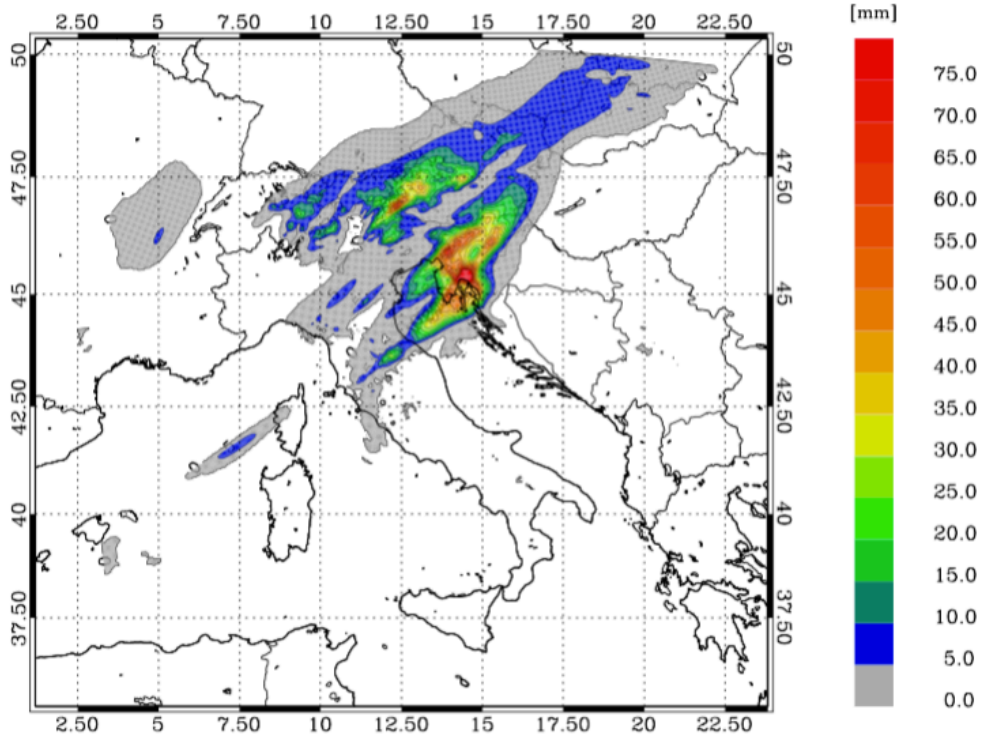
1203

1204

1205

1206   d)

1207
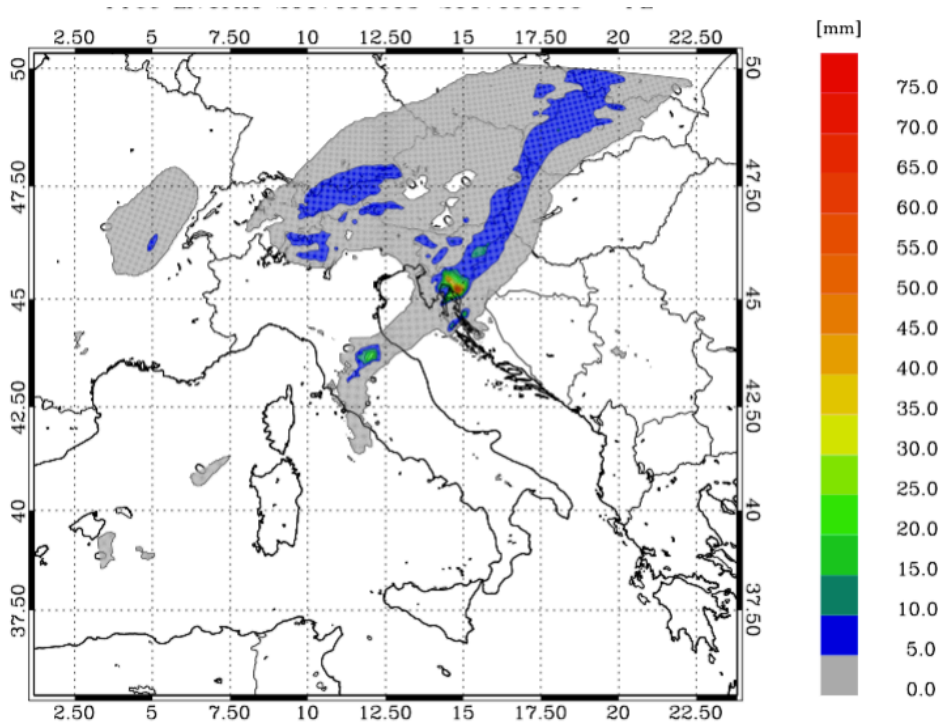
1208

1209

1210   e)
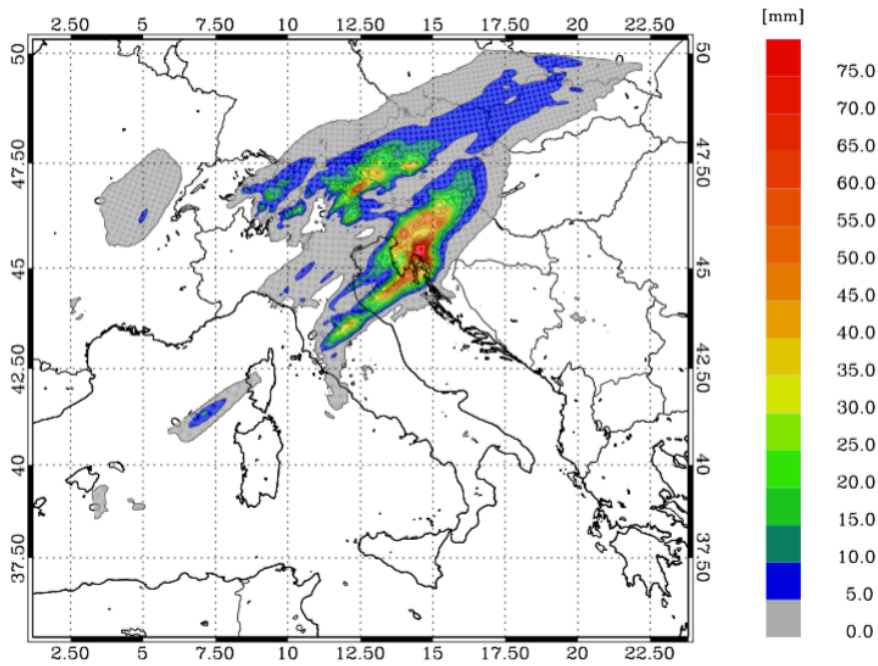
1211

1212   f)
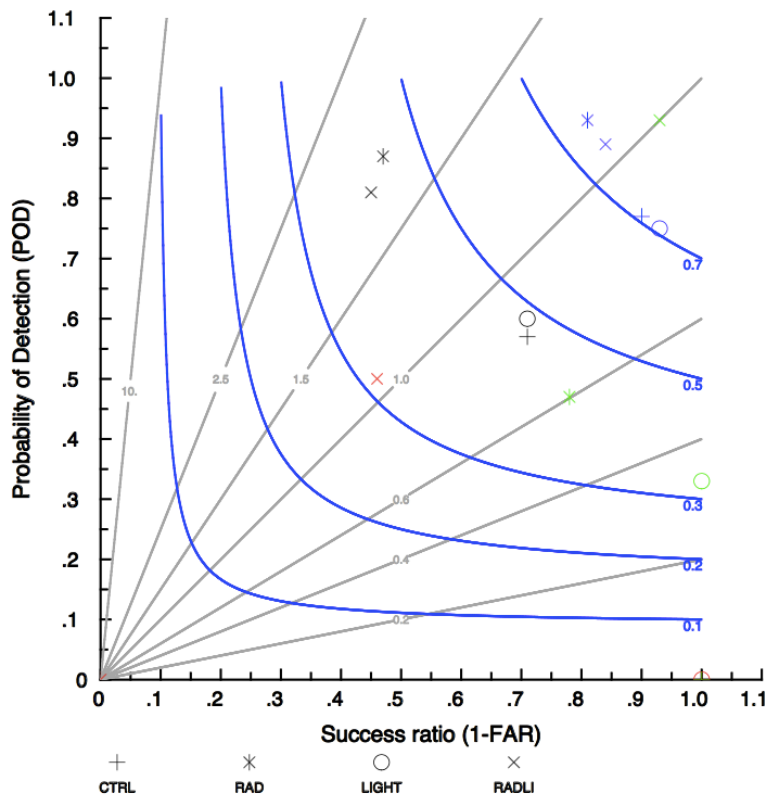
1213

Figure 15: a) rainfall reported by raingauges between 03 and 06 UTC on 16 September 2017. Only raingauges observing at least 0.2 mm/3h are shown. The first number in the title within brackets represents the available raingauges, while the second number represents those observing at least 0.2 mm/3h; b) rainfall VSF of CTRL for the same time interval as in a); c) as in b) for RAD forecast; d) as in b) for LIGHT forecast; e) as in b) for RADLI forecast; f) performance diagram: black symbols are for the nearest neighbourhood and for 1mm/3h threshold; red symbols are for the nearest neighbourhood and for 30 mm/3h threshold; blue symbols are for 25 km neighbourhood radii and for 1 mm/3h threshold; green symbols are for 25 km neighbourhood radii and for 30 mm/3h threshold.

1221

1222   a)
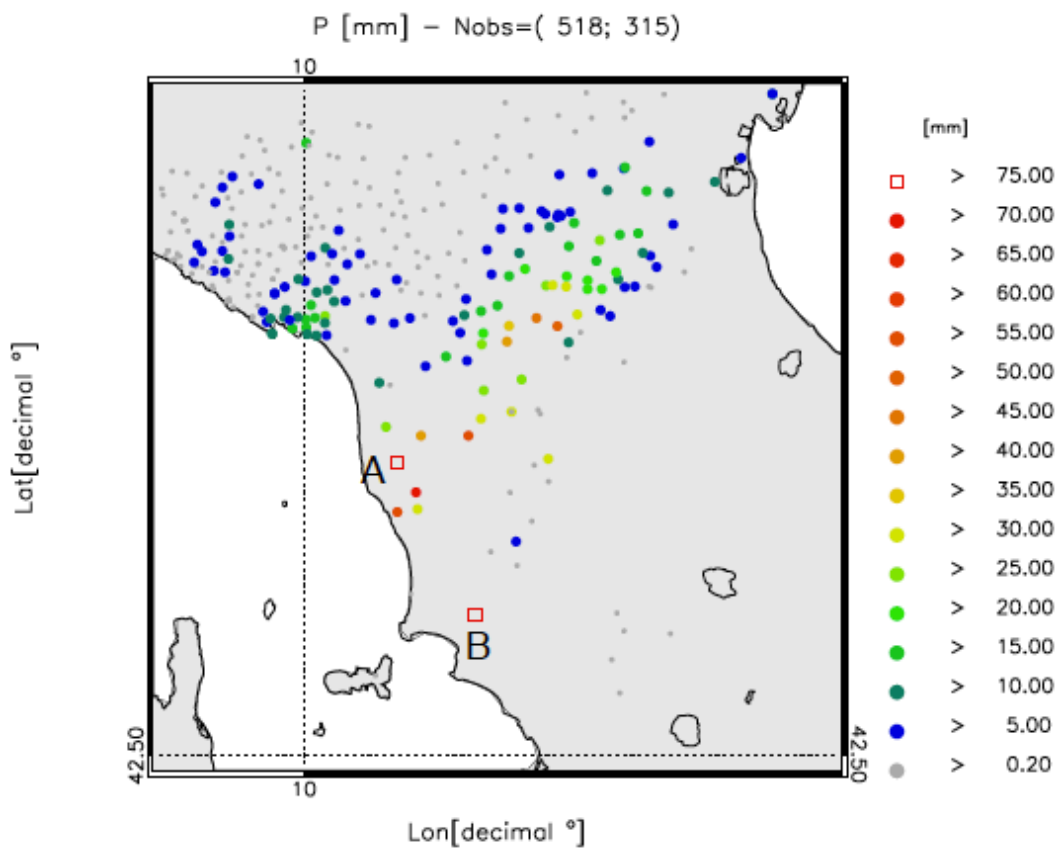
1223

1224   b)
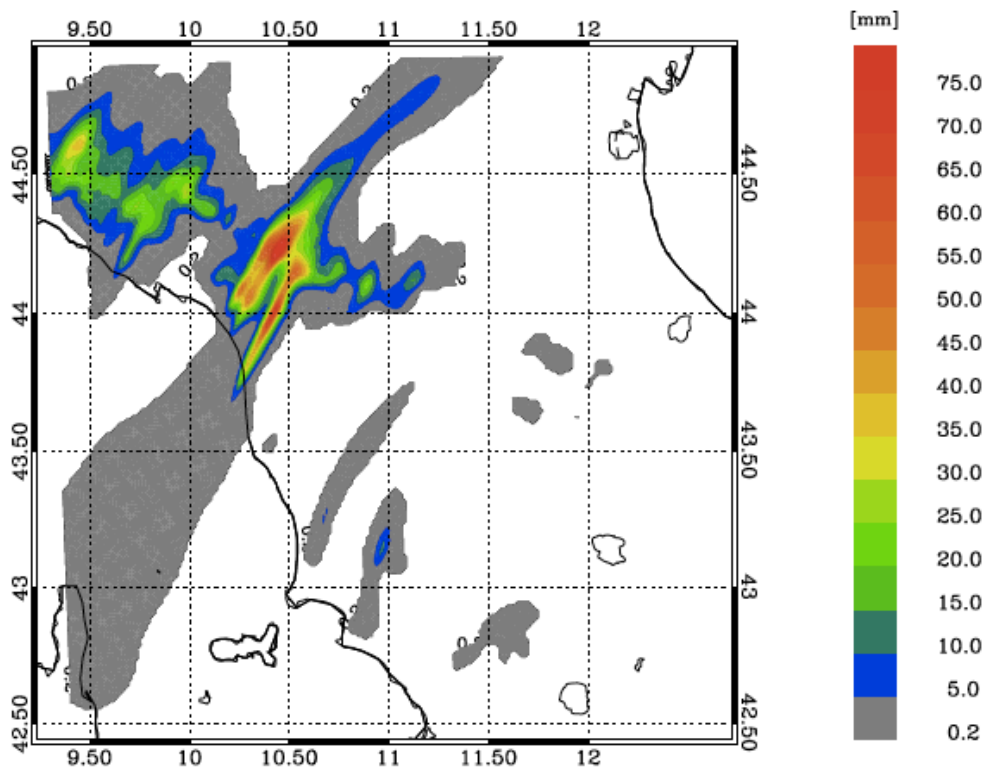
1225

1226

1227

1228   c)
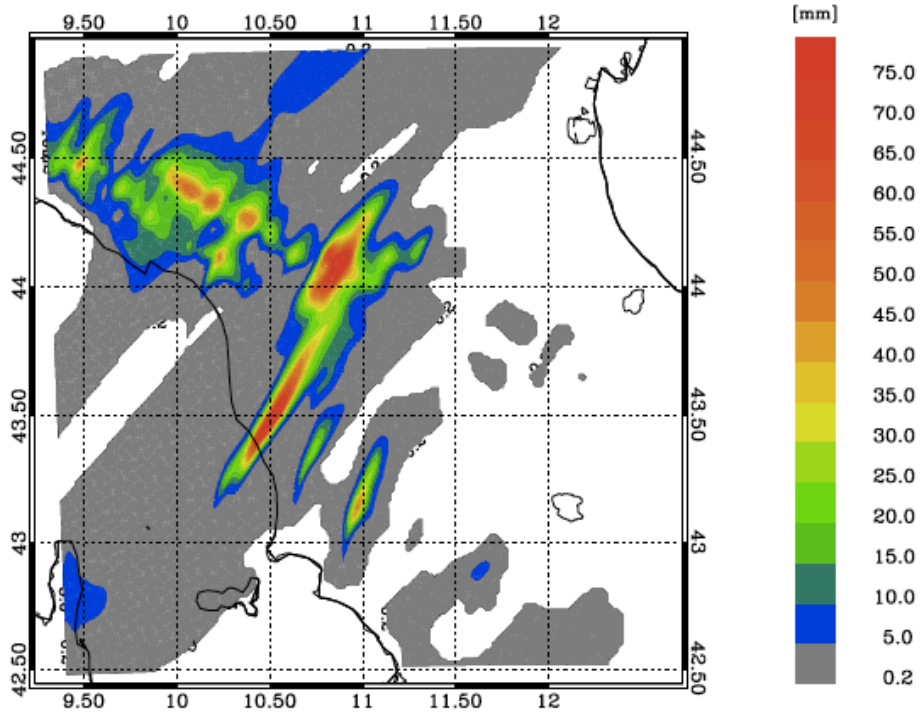
1229

1230

1231   d)
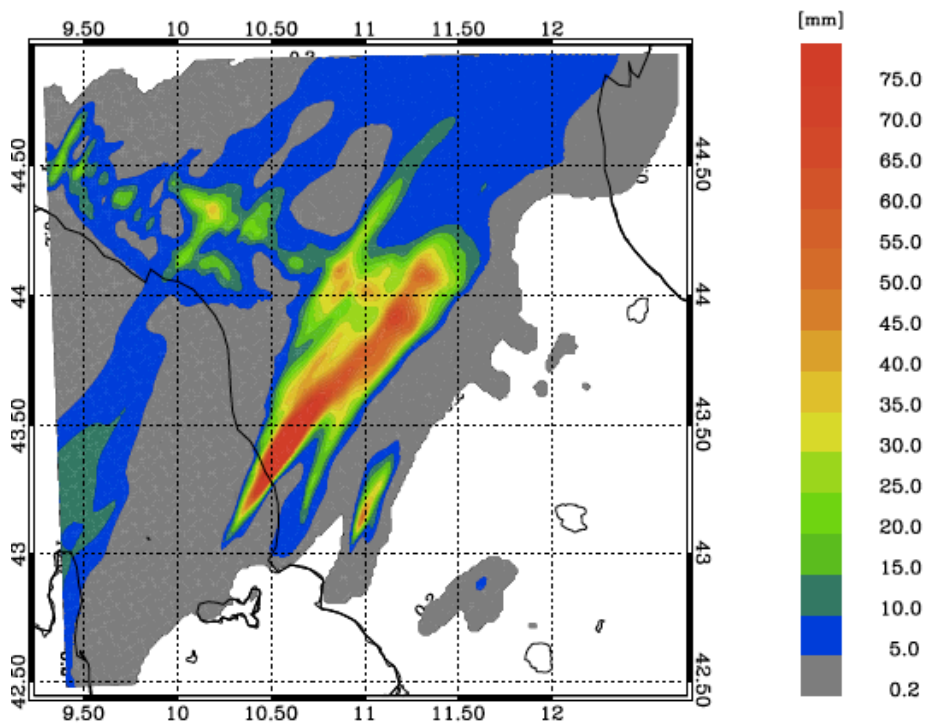
1232

1233

1234

1235

1236

1237   e)

1238
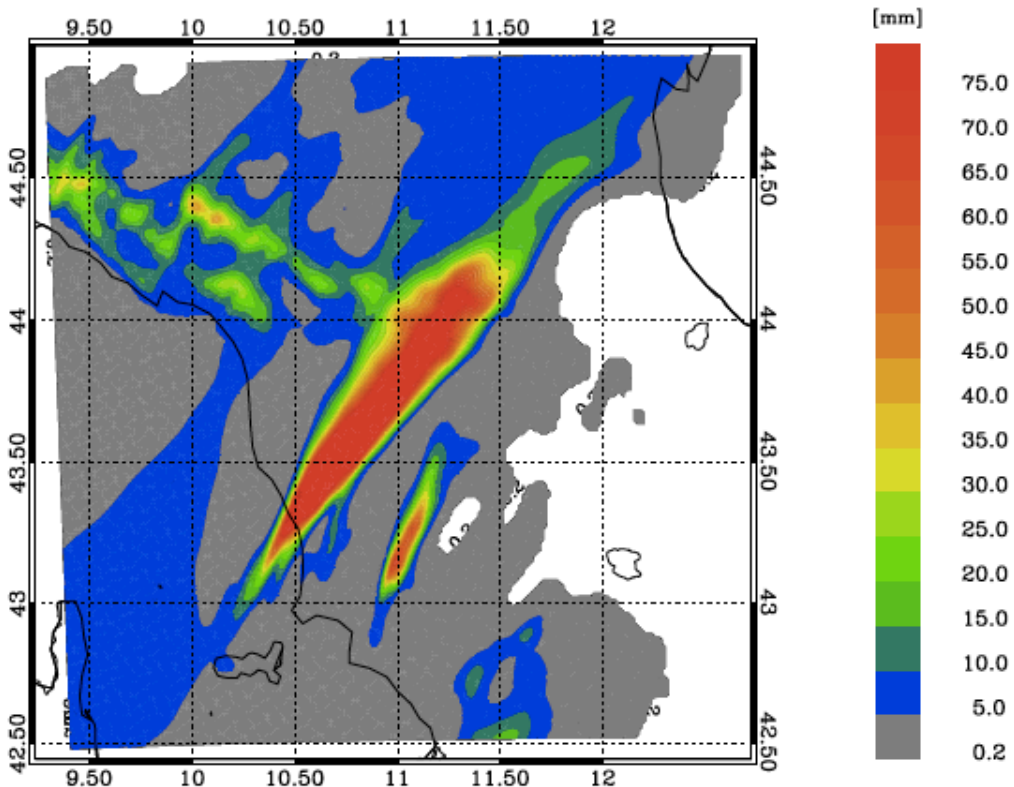
1239

1240   f)
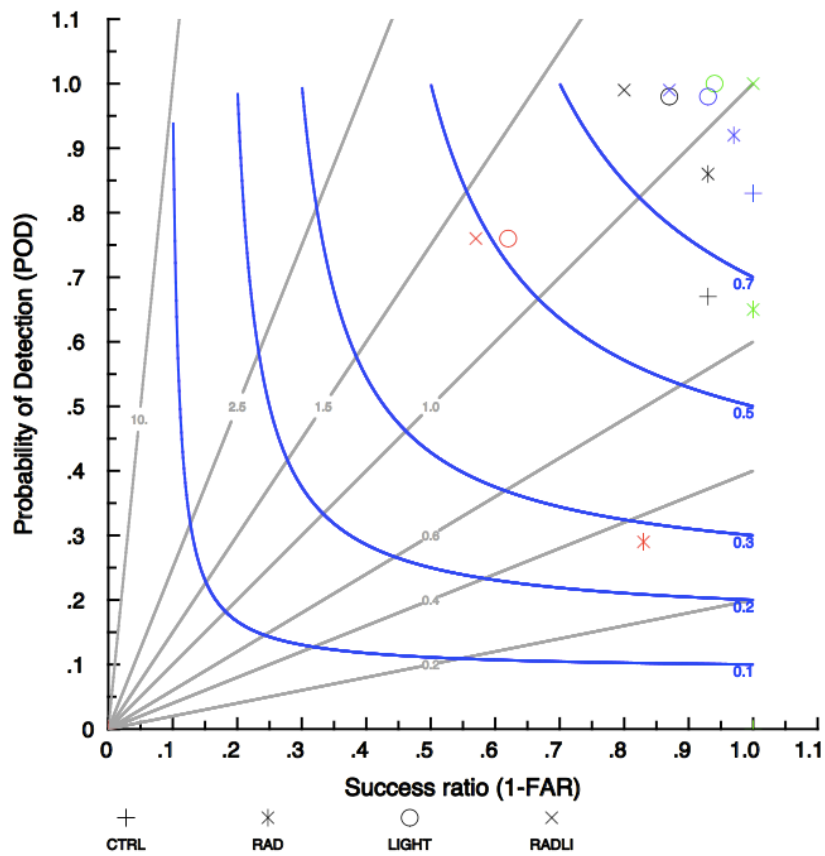
1241
1242

Figure 16: a) rainfall reported by raingauges between 00 and 03 UTC on 10 September 2017. Only stations reporting at least 0.2 mm/3h are shown. The first number in the title within brackets represents the number of raingauges available over the domain, while the second number shows those observing at least 0.2 mm/3h; b) rainfall VSF of CTRL for the same time interval as in a); c) as in b) for RAD forecast; d) as in b) for LIGHT forecast; e) as in b) for RADLI forecast. Labels A and B help to identify the positions of two rainfall maxima discussed into the text; f) performance diagram: black symbols are for the nearest neighbourhood and for 1mm/3h threshold; red symbols are for the nearest neighbourhood and for 30 mm/3h threshold; blue symbols are for 25 km neighbourhood radii and for 1 mm/3h threshold; green symbols are for 25 km neighbourhood radii and for 30 mm/3h threshold.

1295   a)
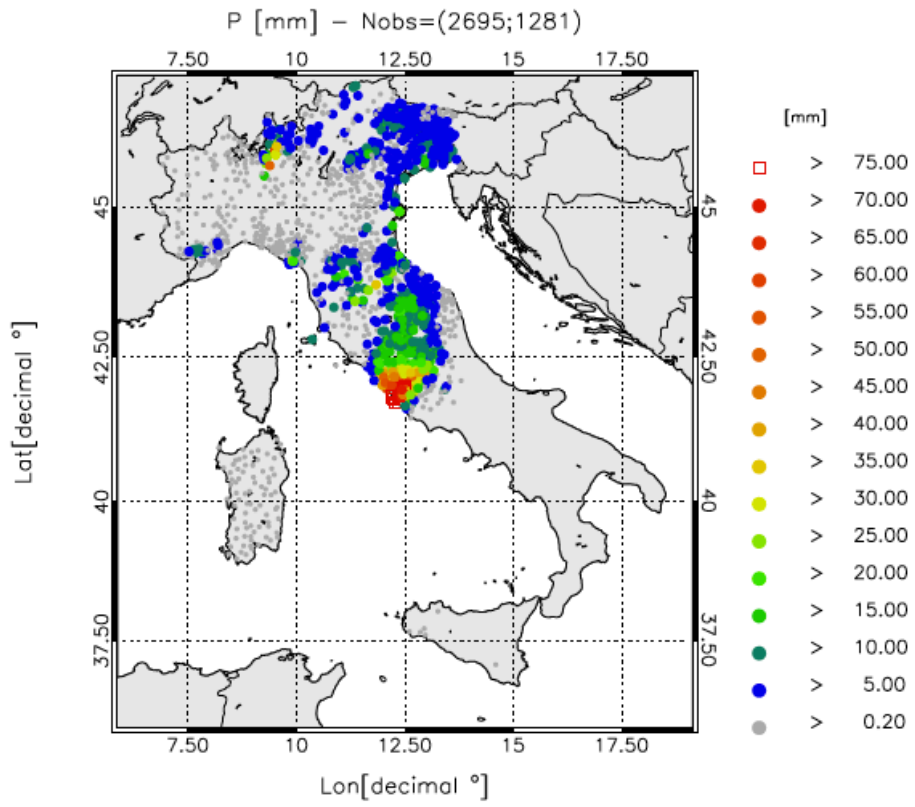
1296

1297   b)

1298
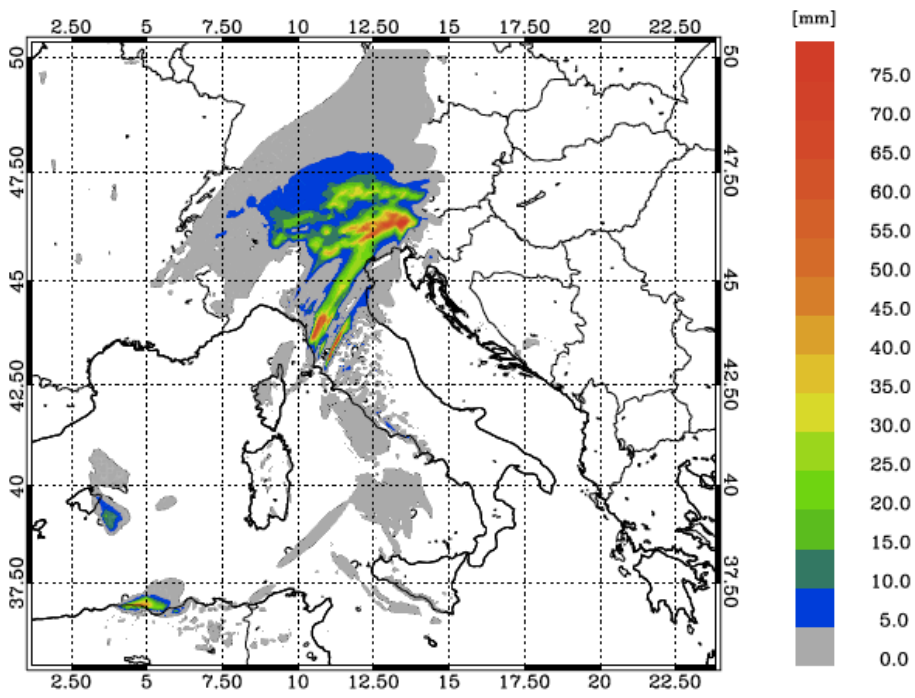
1299

1300

1301

1302

1303   c)
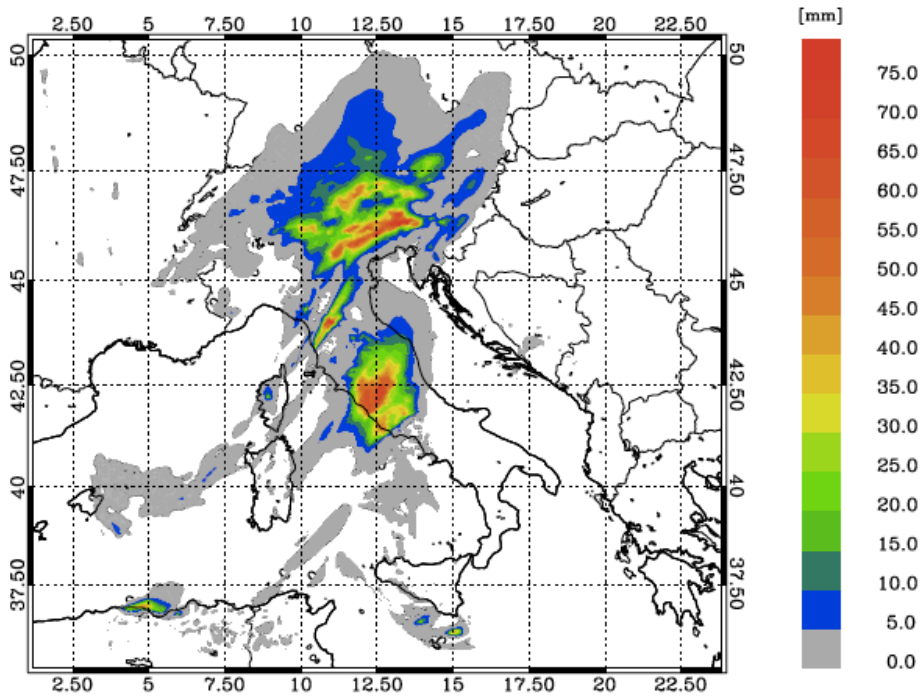
1304

1305

1306   d)
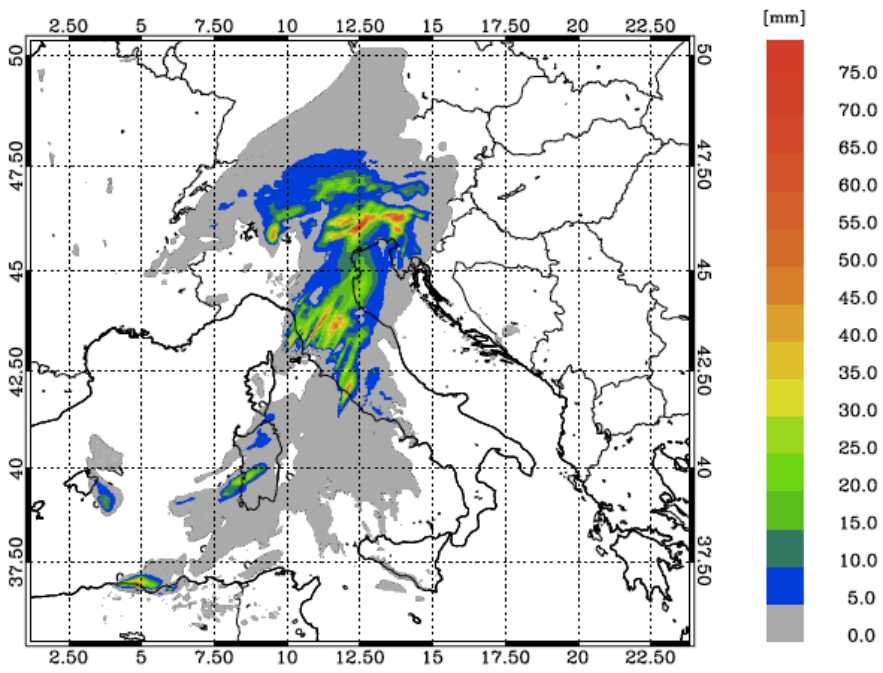
1307

1308

1309

1310

1311

1312

1313   e)
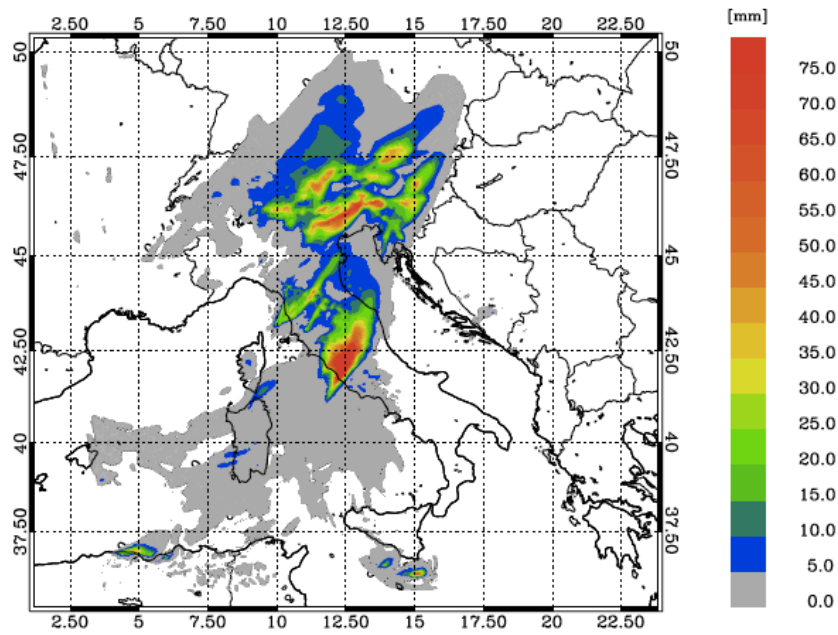
1314

1315

1316   f)
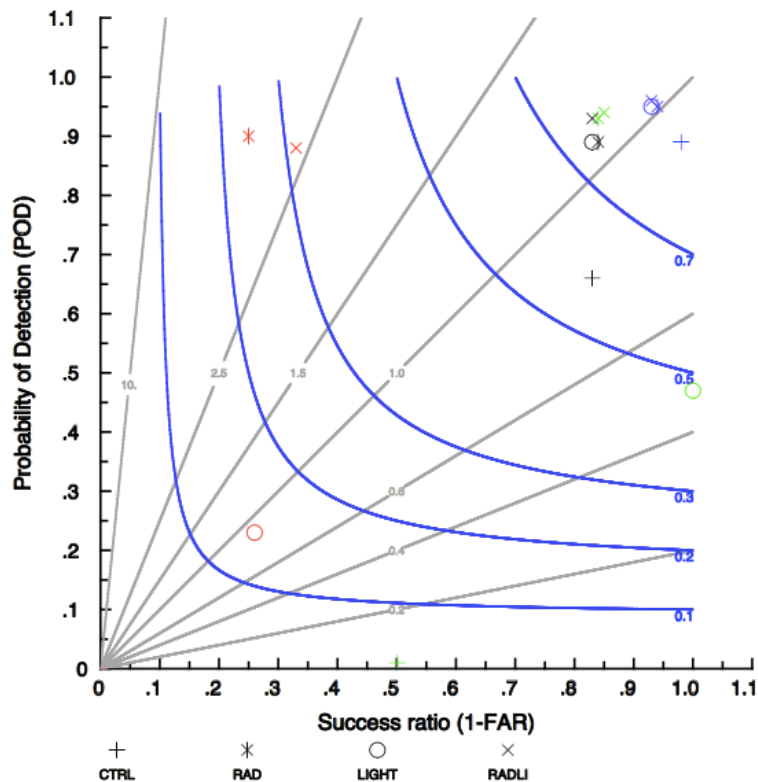
1317
1318
1319   Figure 17: a) rainfall reported by raingauges between 06 - 09 UTC on 10 September 2017. For this time period 2695
1320   raingauges reported valid observations in the domain, however only stations reporting at least 0.2 mm/3h are shown
1321   The first number in the title within brackets represents the number of raingauges available over the domain, while the
1322   second number shows those observing at least 0.2 mm/3h; b) rainfall VSF of CTRL in the same time interval as a); c) as
1323   in b) for RAD forecast; d) as in b) for LIGHT forecast; e) as in b) for RADLI forecast; f) performance diagram: black symbols
1324   are for the nearest neighbourhood and for 1mm/3h threshold; red symbols are for the nearest neighbourhood and for
1325   30 mm/3h threshold; blue symbols are for 25 km neighbourhood radii and for 1 mm/3h threshold; green symbols are
1326   for 25 km neighbourhood radii and for 30 mm/3h threshold.

1327
1328   a)
1329
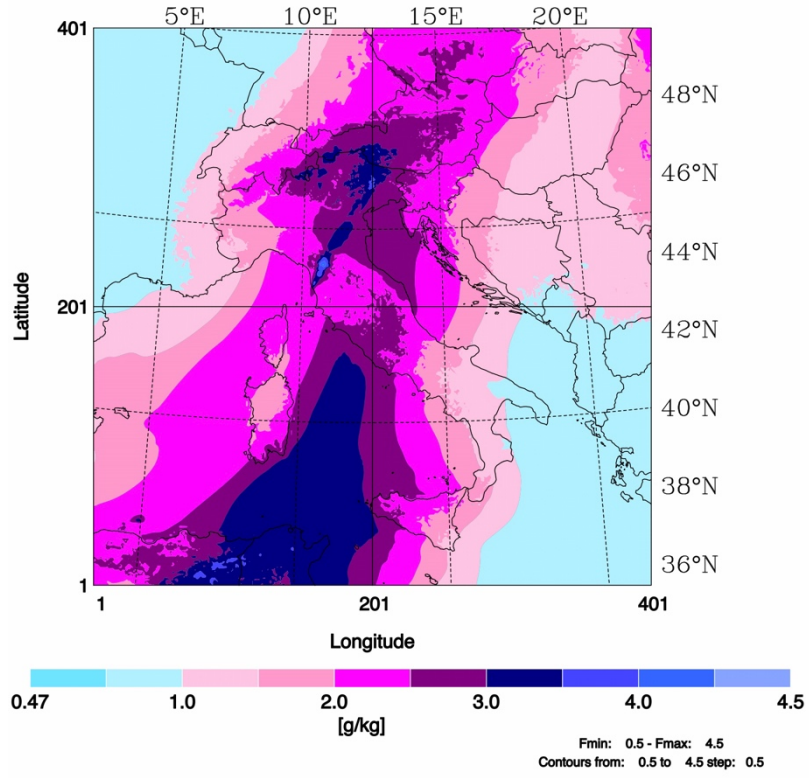
1330
1331
1332   b)
1333
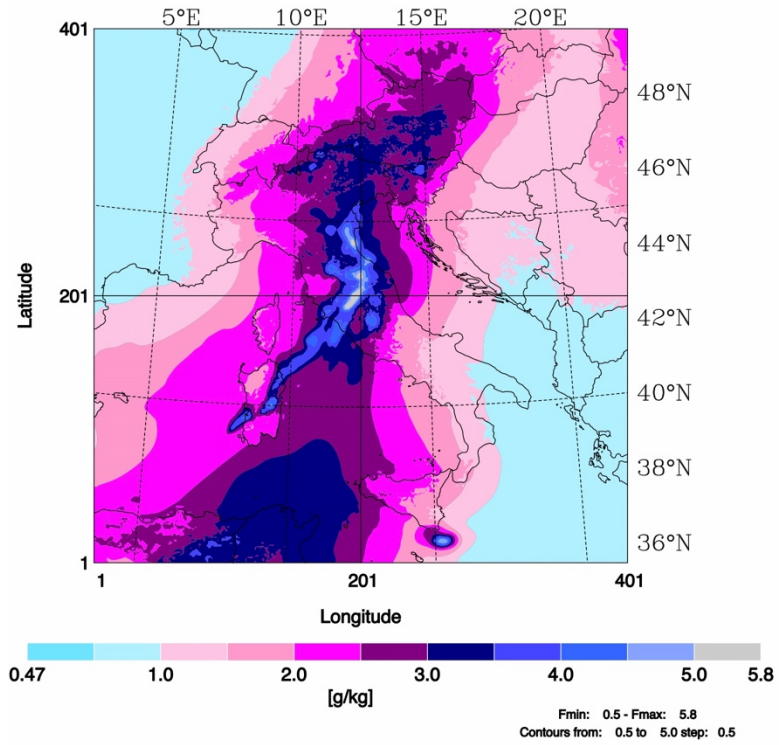
1334
1335
1336   c)
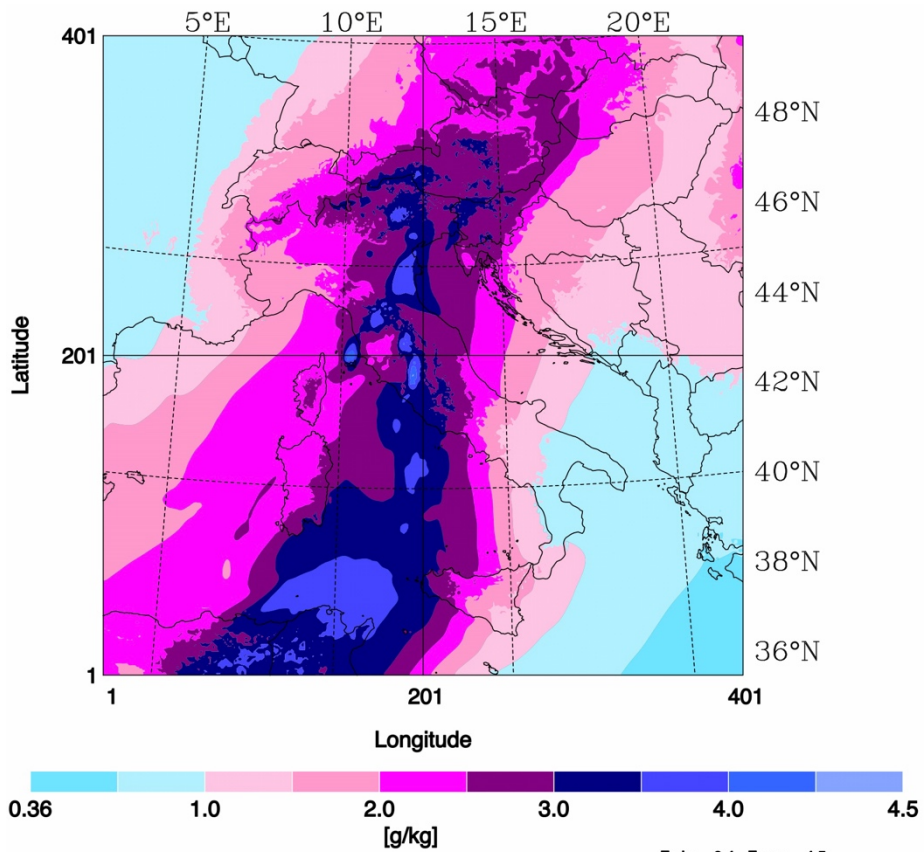
1337
1338   d)
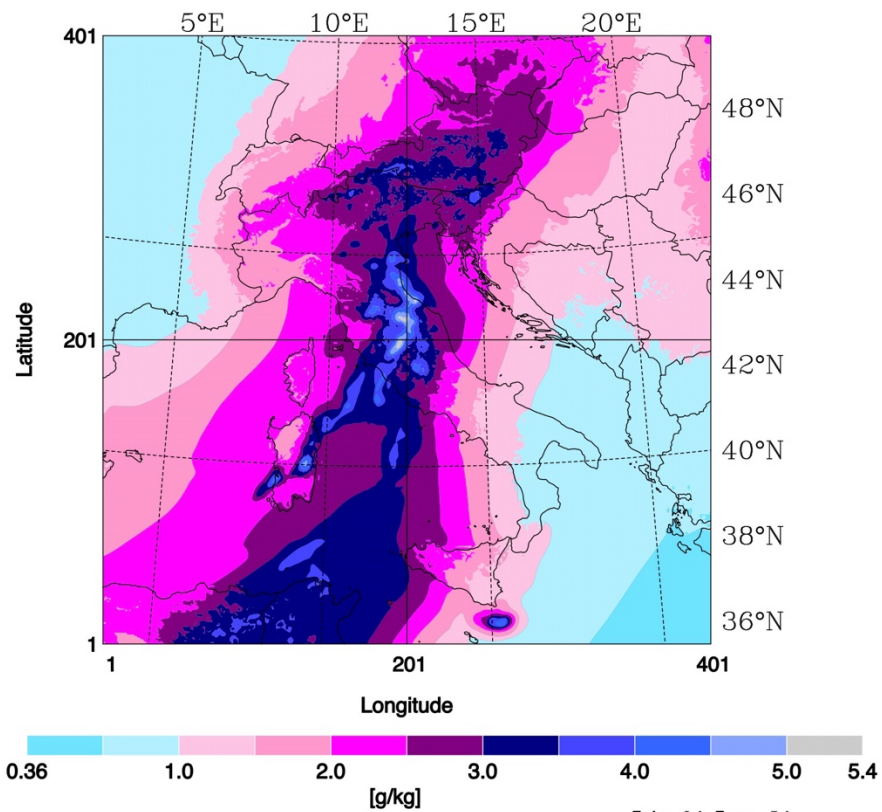
1339
1340
1341   Figure 18: Water vapour mixing ratio averaged between 3 and 10 km at 06 UTC on 10 September
1342   2017 for: a) CTRL; b) RAD; c) LIGHT; d) RADLI.

1343   a)
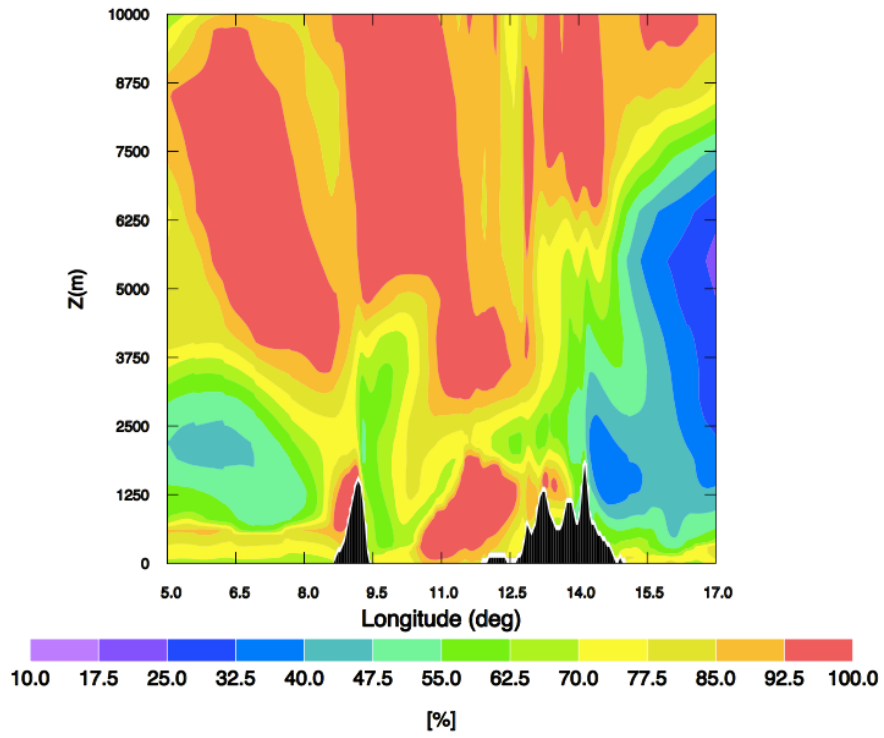
1344
1345
1346   b)
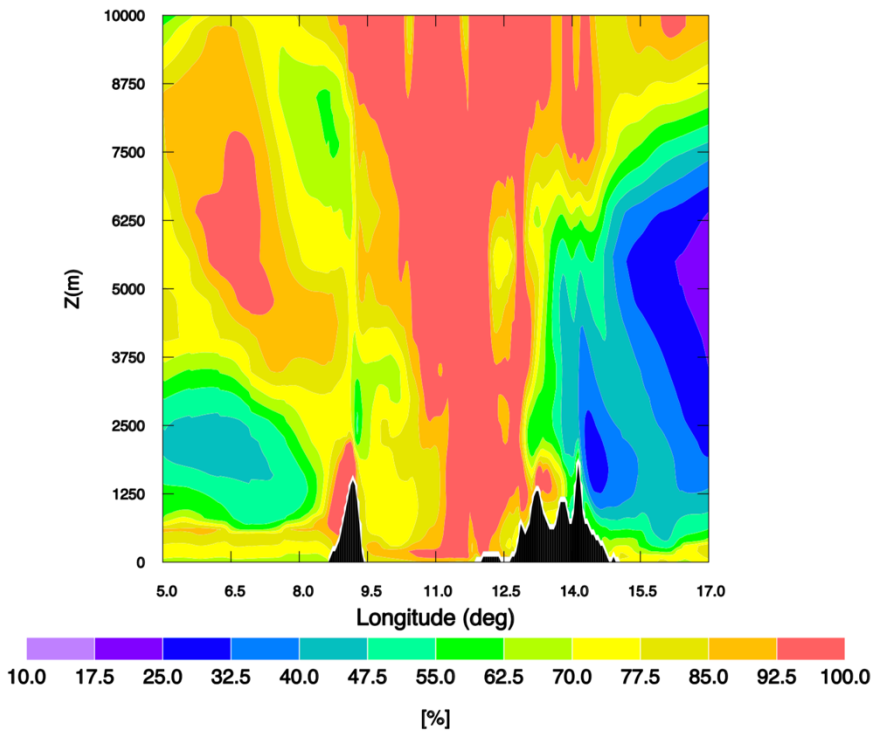
1347
1348
1349
1350
1351
1352
1353

1354   c)
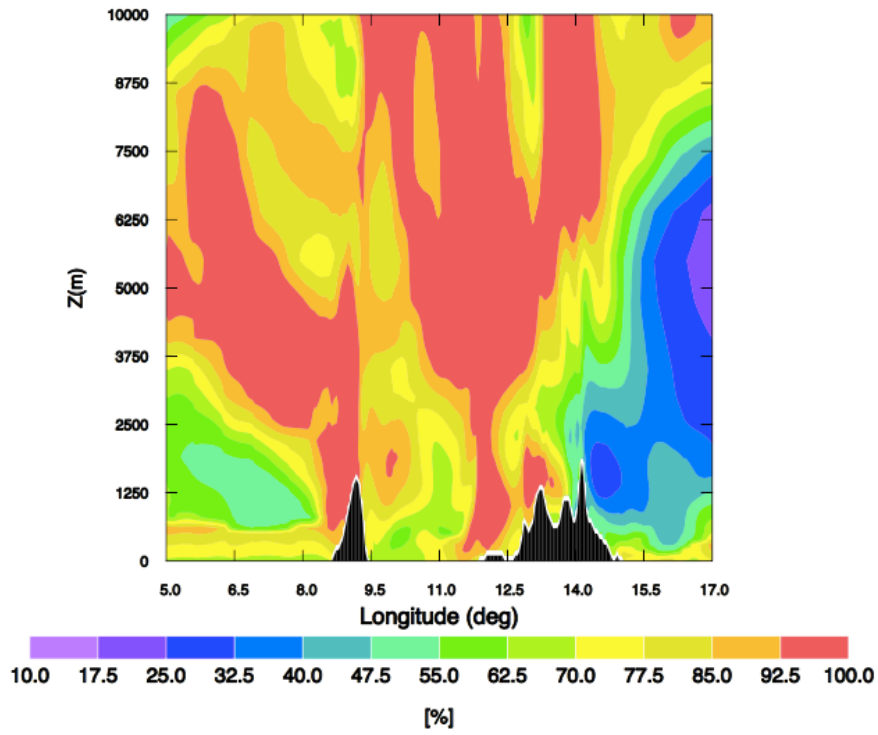
1355
1356
1357   d)
1358
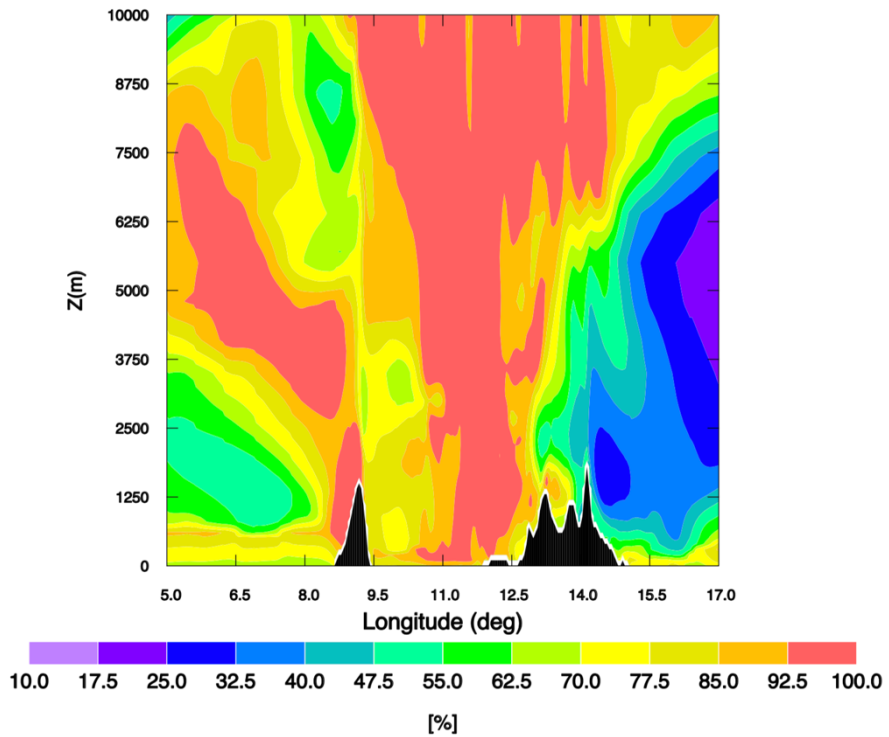
1359
1360
1361
1362   Figure 19: Relative humidity longitude-height cross-section at 42°N and at 06 UTC on 10
1363   September 2017 for: a) CTRL; b) RAD; c) LIGHT; d) RADLI. Only the longitude range between 5 E
1364   and 17 E and the vertical range between 0 and 10 km are shown for clarity.